Institut für Physik und Astronomie
Arbeitsgruppe Nichtlineare Dynamik (AGNLD)
Planetologie

How does adhesion influence the small aggregates in Saturn's rings

Dissertation zur Erlangung des akademischen Grades "doctor rerum naturalium" (Dr. rer. nat.) in der Wissenschaftsdisziplin Theoretische Physik eingereicht an der Mathematisch–Naturwissenschaftlichen Fakultät der Universität Potsdam

von
Ana Helena Fernandes Guimarães

Potsdam
2012

Published online at the
Institutional Repository of the University of Potsdam:
URL http://opus.kobv.de/ubp/volltexte/2012/6184/
URN urn:nbn:de:kobv:517-opus-61846
http://nbn-resolving.de/urn:nbn:de:kobv:517-opus-61846

Curriculum

Ana Helena Fernandes Guimarães

Birth 15.04.1979 - Guaratinguetá, São Paulo, Brazil

Filiation João Ferraz Guimarães and
Maria Aparecida Mendes Fernandes Guimarães

Education *Master in Physic* at University of State of São Paulo "Júlio de Mesquita Filho" (UNESP/Guaratinguetá) - Theme: "Regiões de estabilidade no sistema Plutão-Caronte" (Stables regions around Pluto-Charon System).

Period: 2004-2006
Scholarship holder of FAPESP (Fundação de Amparo à Pesquisa do Estado de São Paulo)

Graduated in *Civil Engineer* at University of State of São Paulo "Júlio de Mesquita Filho" (UNESP/ Guaratinguetá) Theme: "Concreto de Alto Desempenho com Materiais da Região do Vale do Paraíba." (High Performance Concrete with materials from the Paraíba Valley).

Period: 1998 - 2003
Remark: 2^{nd} position in general classification on the course of Civil Engineering.
Scholarship holder of CNPq and FAPESP for scientific initiation.
Scholarship holder as Exchange student of UNESP x Fachhochshule Regensburg in Germany (Aug./2002 Jun./2003).

Further details at
http://lattes.cnpq.br/8510122621636937

To my parents and Daniel.

Acknowledgements

First of all, thank you God for Your help during these years, without faith nothing would be possible.
My thanks go out to the reviewers of this Thesis, especially my supervisor Prof. Dr. habil. Frank Spahn. I am glad to have had the opportunity to write my PhD thesis at the University of Potsdam.
Without the financial support of CAPES, DAAD and the Universität Potsdam this work would not have been possible, thank you.
Further thanks go to the employees of the Univesität , especially my close colleagues Jörg-Uwe Tessmer, Birgit Voigt, Marita Dörrwand, Marlies Path, Andrea Brockhaus, Volker Gustavs, and Claudia Rößling.
Thanks to Nikolai Brilliantov and Ernesto Vieira Neto for their support at the beginning of this work and to Silvia Maria Giuliatti-Winter and Othon Cabo Winter for helping me to come to Germany for my PhD. Many thanks Nicole Albers and Martin Seiß for, besides being great friends, contributing with good ideas to this piece.
Thanks Miodrag Sremčević for providing part of the simulations of aggregates we presented here, enriching the thesis.
I would also like to thank all the “ringlets” for their support and the warm-hearted atmosphere in the group, especially Kai-Lung Sun and Kiri Mochrie, my office-mates, and the Tea-drinking team. And I also thank the “heart-ringlets” Martin Makuch and Eike Jamrath.
Thank you Potsdamer friends- Lucia and Tibor Tyralla, Marcela Makuchova, Claudia Seiß, Steffanie Weber, Marcus Gellert, and the good hearted couple, Anja Reuther and Holger Hoffmann - you all contributed to a friendly enviroment. I also thank my small-big friends Amelie, Annika, Tomasko, Ema, Jana and Julia - life is easier the more colors are around you. Thanks to my Regensburger friends for your, always warm, welcome back: Marion König, Wolfgang Wiesnet, Heloísa Schlingloff, Marta Stock and, especially, Professor Wolfram Weyrauch for all his kind words.
Thanks to my parents, Maria Aparecida and João Guimarães, for their emotional support and warm welcome home during my visits. Thank you uncle Aluísio, aunts Dulce and Luzia. Thanks: Rômulo, Iara, Bia, Lukas, Eliana, Antônio, Nilza, João Paulo, Mariana, Silvinha, Maria Geni, Ana Lúcia, and Eleonara for visiting me here. Also thanks for the visits of Pierre and Pedro Kaufmann, and Rodopho Vilhena de Moraes. Thanks to all my family members, which belong to a long list of good friends, for keeping in touch. Thanks to my brazilian friends for being there for me.
Finally, special thanks to my love Daniel Kreppel for supporting me with all his heart and for crossing the ocean many times to see me. Thanks also to the Skype support team for making the distances shorter.

“ L’homme se découvre quand il se mesure avec l’obstacle. ”
(Antoine de Saint Exupéry)

Contents

CONTENTS

List of Figures

LIST OF FIGURES

Glossary

$\bar{\gamma}$	average adhesion energy density
γ	twice the surface free energy
γ_0	surface free energy
$\hat{N}$	number of constituents in unit cell
ν	Poisson ratio
Ω	mean motion
ρ	density of the constituent material
ρ_{agg}	density of the aggregate
A	pre-factor from the adhesion energy
C	total number of contacts
C_N	coordination number (number of contacts of a single constituent)
D	combined bulk material constants
E_A	adhesion energy
E_G	gravitational self-energy
E_T	total self-energy given as $E_T = E_G + E_A$
$E_{fragment}$	energy of a fragment during the breaking process
f	filling factor of an aggregate
$f(\tilde{R})$	fragment size distribution
G	gravitational constant
g	relative velocity
g'	post-collisional relative velocity
g_c	relative critical velocity where the aggregate neither grow nor shrink
g_m	aggregate relative mean impact velocity
g_{frag}	critical fragmentation relative velocity
M	aggregate total mass
m	mass of a single constituent particle
M_{eff}	effective mass of two aggregates
N	number constituent particles
N_{u}	number unit cells
Q	specific self-energy (energy per mass)
$Q^\star$	specific break up energy, threshold energy required to break an object such that the largest fragment has half the mass of the original body
Q_A	specific adhesion energy
Q_G	specific gravitational self-energy
R	aggregate radius
R_c	characteristic radius, denotes the radius of a homogeneous sphere
R_g	gyration radius
R_m	this is a critical (minimal) radius size for the projectile (the smaller aggregate) to always fragment the collisional partner aggregate
R_t	transition radius size which an aggregate is more likely to be destroyed
S	new surface area after breakage
s	radius of a constituent particle
s_0	radius for equal sized particles
v_{th}	thermal velocity
W_{A}	denotes the work done to create new surfaces
W_{G}	is the work done to physically separate the fragments within their own gravitational field
Y	Young's modulus

Abstract

Particles in Saturn's main rings range in size from dust to even kilometer-sized objects. Their size distribution is thought to be a result of competing accretion and fragmentation processes. While growth is naturally limited in tidal environments, frequent collisions among these objects may contribute to both accretion and fragmentation. As ring particles are primarily made of water ice attractive surface forces like adhesion could significantly influence these processes, finally determining the resulting size distribution. Here, we derive analytic expressions for the specific self-energy Q and related specific break-up energy $Q^\star$ of aggregates. These expressions can be used for any aggregate type composed of monomeric constituents. We compare these expressions to numerical experiments where we create aggregates of various types including: regular packings like the face-centered cubic (fcc), Ballistic Particle Cluster Aggregates (BPCA), and modified BPCAs including e.g. different constituent size distributions. We show that accounting for attractive surface forces such as adhesion a simple approach is able to: *a)* generally account for the size dependence of the specific break-up energy for fragmentation to occur reported in the literature, namely the division into "strength" and "gravity" regimes, and *b)* estimate the maximum aggregate size in a collisional ensemble to be on the order of a few meters, consistent with the maximum aggregate size observed in Saturn's rings of about 10 m.

Chapter 1

Introduction

It was Galileo Galilei who, in the year of 1610, first observed the remarkable shape of Saturn. He was not able to explain the observed formation, but his discovery raised the interest of the scientific community in the Saturnian system. In 1655 Christian Huygens suggested that the peculiarly shaped planet seen by Galileo was actually a solid ring - the first piece of the Saturn puzzle was solved. The idea of a ring was supported by Giovanni Cassini, and later also by Laplace, Maxwell, Keller and Campell, their studies and calculations showed that the true structure of the rings was that of a myriad of particles and not a solid ring. Because of its ring system, Saturn is a bright spot on the firmament and nowadays, using a binocular telescope, one can see its elliptical silhouette from Earth (Schlingloff, 2005).

All four giant gas planets in our Solar System have rings, but the Saturnian system is extraordinary and has been fascinating scientific minds from earlier centuries until today. Saturn's rings have a far greater mass than the rings of any other ringed planet and although structural phenomena can be observed in the rings of the other planets, it is only Saturn's rings that show the complete diversity of these structures (Cuzzi

et al., 2010). The rings are extremely thin in comparison to their other dimensions, spanning about 140000 km across while being only about 10 m thick. A myriad of particles form this complex ring system, together with a huge number of satellites (see Fig. 1.1). Furthermore, the physics involved in shaping Saturn's rings has parallels with the processes active in protoplanetary disks (Cuzzi et al., 2010), electing this system to be considered as "natural laboratory" in order to study dynamical processes of planet-formation.

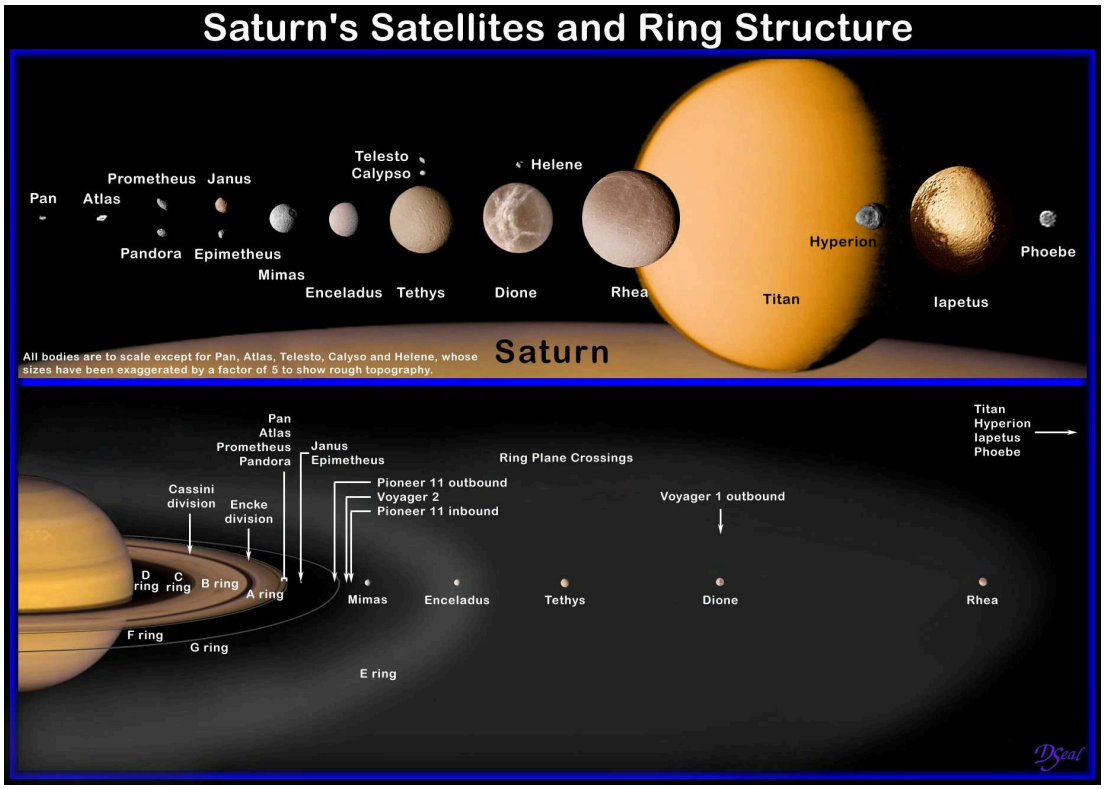

Figure 1.1: This image shows Saturn, its ring structure and satellites to relative scale unless otherwise noted (Artwork by David Seal, P-46507BC NASA images).

For the last three decades our knowledge about Saturn's system has increased enormously, mostly due to the flybys of the spacecrafts Pioneer 11 and the twins Voyagers I and II, but also due to the observations done by Hubble Space Telescope (Murray and Dermott, 1999; Dougherty et al., 2009). Today research into the dynamics and kinetics

of planetary rings, specifically the magnificent rings of Saturn, is strongly supported by the successful Cassini spacecraft[1]. Cassini is the fourth space probe to visit Saturn and the first to orbit the planet (see Fig. 1.2 - a marvelous view taken by the space probe).

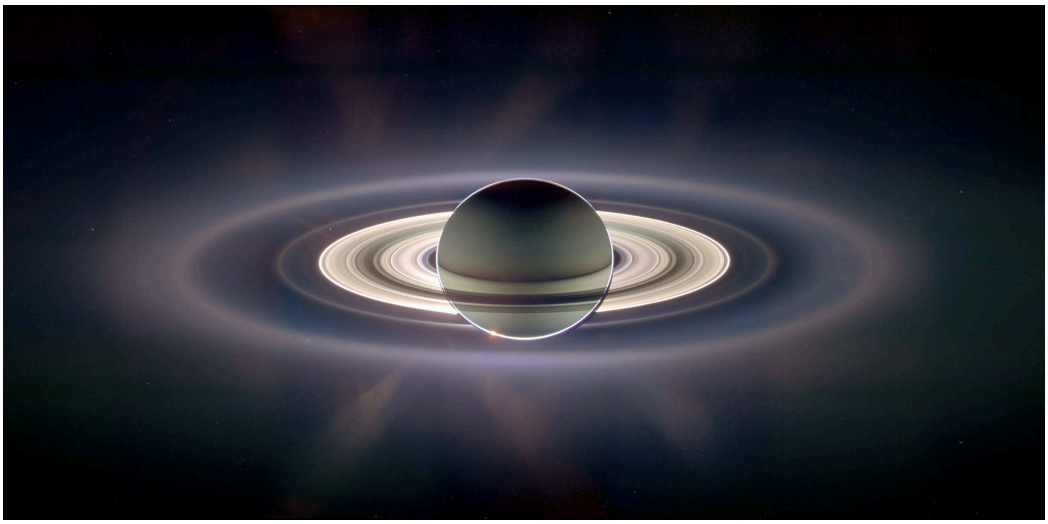

Figure 1.2: This image is a marvelous panoramic view created from Cassini data in September 2006. It was taken at high phase angle, i.e., the sun is almost directly behind Saturn, and therefore the dust particles brighten substantially. Working outward from the planet, the rings are divided in two groups: D, C, B, and A, the major ring groups; F, G, the fainter and narrower rings, and the big dust E ring (PIA08329 from NASA images).

New discoveries by these missions have increased the ongoing debate about the formation of planetary rings. There are two major theories about their origin, so far neither of them could be singled out. One scenario regards the ring particles to be remnants from the formation of the giant planets and their satellites (accretion). In this case they would be the witnesses of Saturn's birth about 4.5 billion years ago: the single pieces being remnants of satellites that failed to form (Esposito, 2002). The alternative theory considers the destruction of a parent body (e.g a satellite, or a comet, or an asteroid), a strong collisional impact could have led to the disruption of the impactor

[1]Cassini-Huygens Mission, launch 1997 - arrived at Saturn in 2004. In 2008 a two-year extension was announced, at which point it was renamed to Cassini Equinox Mission. The second extension was in February 2010 with the Cassini Solstice Mission continuing until 2017.

and the debris formed the planetary rings. The discovery of the building-sized moonlets in Saturn's A ring by Tiscareno et al. (2006) and Sremčeivć et al. (2007) tends to favor the latter scenario rather than a co-genetic origin with Saturn, since bodies of this size can hardly have accreted inside the rings due to the tidal work – as argued by e.g. Sremčević (2007), Spahn and Schmidt (2006) and others. For both cases the solution to the puzzle of ring origin must consider the recycling of ring material (Dougherty et al., 2009). The origin of the rings is still subject of discussion and remains open.

Ring particles are believed to be aggregates of smaller particles arranged into transient elongated clumps (*see* Fg. 1.3). Different ring regions may have been formed from different progenitor bodies and therefore could be of different ages (Porco et al., 2007; Dougherty et al., 2009). It has long been known that water ice constitutes the bulk of the ring material. Moreover, Cuzzi et al. (2009) comment that the particle composition evolves with time due to environmental factors such as irradiation by photons, and/or collisions with interplanetary meteoroids. Interplanetary debris is primarily non-icy material silicates and carbon rich organics – so the rings become increasingly "polluted" over their lifetime.

This thesis mainly considers the massive rings of Saturn (A,B,C and Cassini division), where collisions among the ring particles are frequent and the observed size distribution is likely to be the result of the balance between coagulation and fragmentation processes (Longaretti, 1989; Barbara and Esposito, 2002; Spahn et al., 2004; Esposito et al., 2011).

In general, agglomeration (coagulation)^2 of small ring particles (constituents) may create larger ones (agglomerate), while fragmentation (fission or disruption) would, naturally, limit this growth. However, fragmentation may occur not only due to collisions but also due to tidal stresses (Davis et al., 1984). The dense ring perturbed regions

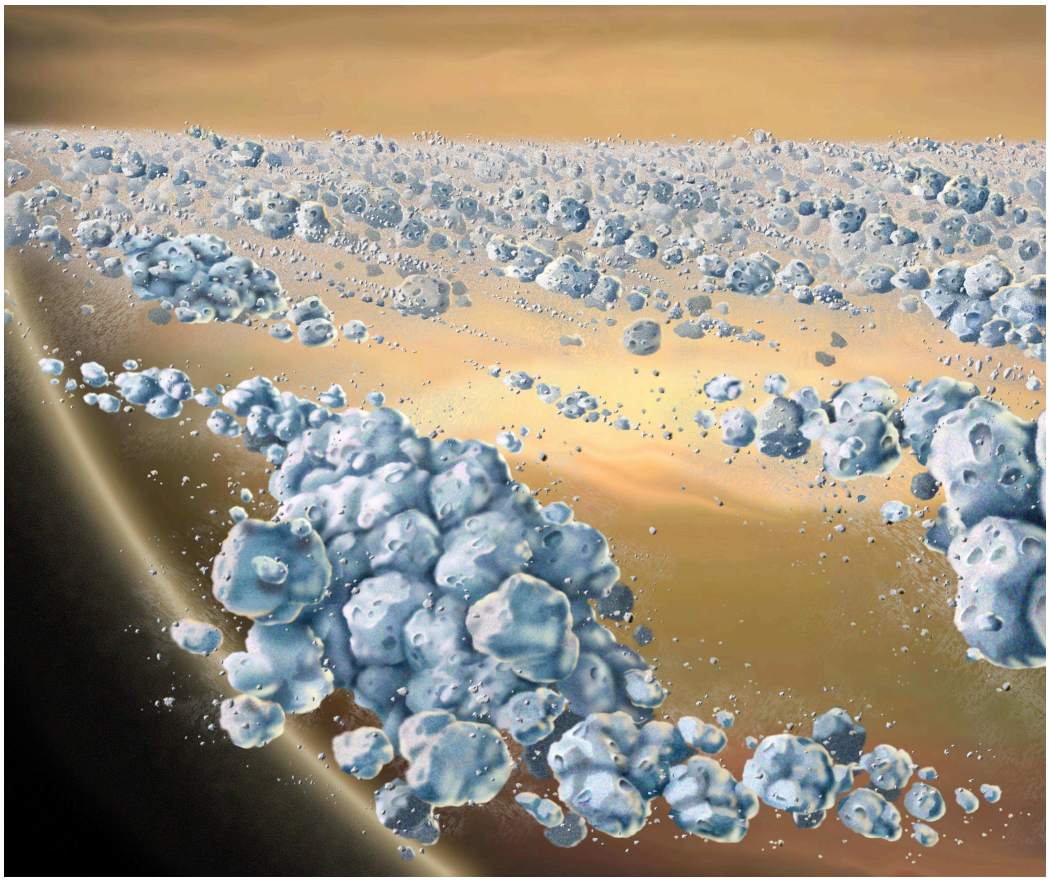

Figure 1.3: The particles (blue) are composed mostly of ice, but are not uniform. They clump together to form elongated, curved aggregates, continually forming and dispersing. They are the called “Dynamical Ephemeral Bodies”, particles might temporarily aggregate into larger bodies and are eventually sheared apart again by dynamical forces in the rings or collisions. (Artwork by Marty Peterson, based on a 1984 image by William K. Hartmann, PIA10081 NASA images.

is favorable to aggregate formations. For example, near the regions of propeller belts within the ring (Tiscareno et al., 2006; Sremčeivć et al., 2007) or also halos around strong resonant waves – in both cases, propeller and waves, the perturbed area appears brighter in reflected light (Hedman et al., 2007). This is because such perturbations cause larger collisional speeds, delivering smaller ring particles from surface of larger ones and, in this way, the particle size distribution (Bodrova et al., 2012).

Another hint for aggregates being the building blocks of Saturn’s rings comes from ob-

servations. They show that ring particles (aggregates) are under-dense ($\simeq 400\,\mathrm{kg\,m^{-3}}$), e.g. by comparing: *(a)* the inferred particle size distribution (Zebker et al., 1985; French and Nicholson, 2000; Marouf et al., 1983) and the surface mass density derived from density wave analysis (Tiscareno et al., 2007), and *(b)* simulations and observations of the self-gravity wakes induced (i) ring brightness asymmetry (French et al., 2007) and (ii) ring optical depth asymmetry (Salo, 1992, 1995; Colwell et al., 2006, 2007; Hedman et al., 2007; Robbins et al., 2009). pointing to self-gravity wakes whose generation requires a certain ring mass to promote the gravitational instability.

In regard of the balance between aggregation and fragmentation, another Saturnian ring that is of interest in this work is the thin and lively F ring, which is strongly stirred by its shepherd satellites (Murray et al., 2005), Prometheus and Pandora (see Fig. 1.4). The F ring mainly consists of micrometer sized particles (dust), macroscopic clumps (approximately centimeter to meter sized objects) (Esposito et al., 2008; Meinke et al., 2012), and kilometer sized moonlets (Murray et al., 2008). The latter are most likely transient in nature (Spahn and Sponholz, 1989; Winter et al., 2007; Esposito et al., 2008; Beurle et al., 2010) and chaotically moving in the F ring region. These Dynamic

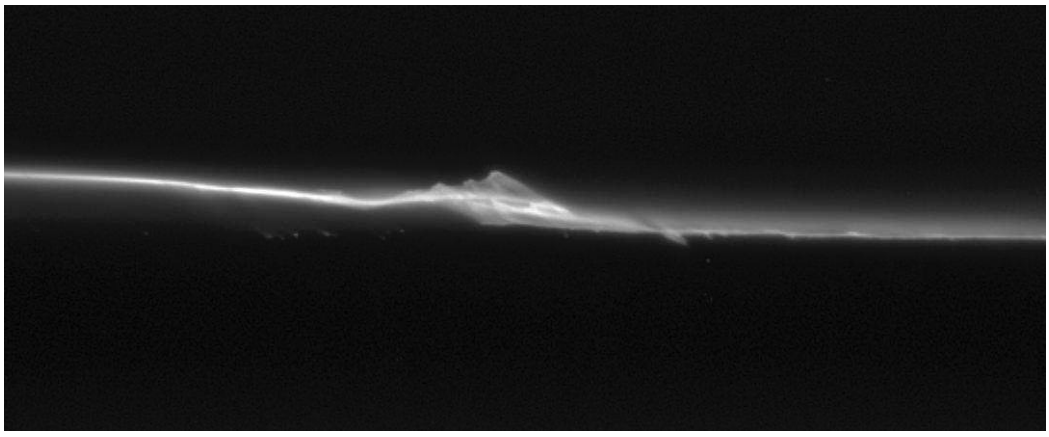

Figure 1.4: The dynamism of F ring – this figure shows prominent jets and spirals probably due to recent collisions.

Ephemeral Bodies (DEB) (Weidenschilling et al., 1984) could emerge from ongoing

disruptions and re-accretions on dynamical timescales that give this narrow ring its lively appearance. While dissipative collisions ensure the thermal stability of a planetary ring (Goldreich and Tremaine, 1978), relative impact speeds and sizes determine whether coagulation, restitution or fragmentation occurs (e.g. Spahn et al., 2004). The latter outcome can further be sub-classified to include erosion where part of the mass is removed (e.g. Dohnanyi, 1969) or a type of erosion where mass is transferred during a collision with a bouncing outcome (Güttler et al., 2010). Fragmentation, however, is not caused only by collisions, but also by tidal stresses (Davis et al., 1984). In general, agglomeration (coagulation) of small ring particles (constituents) may create larger objects while fragmentation (fission or disruption) would naturally limit this growth.

Small bodies in the Solar System generally show features of strength and their mechanical properties undoubtedly play a major role in their collisional evolution (Holsapple, 2009), where strength (or resistivity) is defined as some measurement of a material ability to withstand particular stresses, strains or loads. In the case of agglomerates the resistivity is defined by the contact forces between the constituents. These bonds are typically broken long before material failure of a single constituent. Seipenbusch et al. (2007) showed that the bond strength between particles (energy per area) arranged in larger objects such as agglomerates is a key parameter for understanding the mechanical properties of these composite materials. Furthermore, the coordination number (number of contacts per constituent) plays a crucial role in determining these properties. In asteroids the resistivity can be divided into a strength-dominated and gravity-dominated regime (Housen and Holsapple, 1990; Love and Ahrens, 1996; Benz and Asphaug, 1999). Typically, resistivity decreases with increasing object size until, above a certain transition size, resistivity increases as the body's own gravitational influence becomes dominant.

1. INTRODUCTION

Similar to asteroids, ring particles are thought to be (rubble piles) loosely bound aggregates. As the ring's velocity dispersion in unperturbed regions is small ($\mathrm{mm\,s^{-1}}$ to $\mathrm{cm\,s^{-1}}$) compared to the orbital velocity ($\mathrm{km\,s^{-1}}$), impacts are generally low-speed, this is favorable for aggregation (e.g. Hatzes et al., 1991). A velocity-dependent coefficient of restitution has been modeled using collision models based on viscoelastic particle interactions (Brilliantov et al., 1996). Taking into account surface adhesion, (Johnson et al., 1971) more recent models are able to consistently model both low-velocity sticking (aggregation[2]) and bouncing between individual particles (restitution) (Albers and Spahn, 2006; Brilliantov et al., 2007) in qualitative agreement with laboratory experiments (Bridges et al., 1984; Hatzes et al., 1991).

In order to quantify the balance between aggregation and fragmentation, we discuss the resistivity and stability of particle aggregates, which are made of multi-constituents and are bound together by short-range adhesive contact and long-range gravitational forces. Adhesive contacts were considered for asteroids by Scheeres et al. (2010) using a similar approach. Here, we show how adhesion modifies the resistivity of these fragile bodies studying its influence for different types of aggregates.

This work is an extension of Albers and Spahn (2006), who demonstrated that objects in the rings as large as 10 m could exist, matching the inferred size of ring particles (Zebker et al., 1985). These estimates are based on orbital dynamics including adhesive forces and collisions – using collisional velocities typical for the ring. However, Albers and Spahn (2006) restricted their study to binary aggregates (*two* constituents). Here we analytically calculate the specific self-energy and resistivity (specific break-up energy) of N-particle aggregates and compare these to numerically created aggregates of

[2]Coagulation, aggregation, and agglomeration are widely used throughout this thesis. In principle, denoting different physical scenarios, they refer to the same thing, i.e. the sticking of grains. Otherwise, coagulation refers to the merging of two droplets, agglomeration refers to the simple accumulation of grains without changing their shape and the only "glue" between them is the self-gravity. Aggregation is similar to agglomeration, but with chemical bonds between the particles (adhesion).

various types such as regular packings, Ballistic Particle Cluster Aggregates (BPCA), and modified BPCA including particle size distributions. We then infer their stability in a collisional regime. We used assumptions for the break-up energy that are qualitatively consistent with previous works, but they are simplistic and do not take fully into account how an aggregate may fracture. We are interested in the energy estimates and want to offer a tool for quick calculations. A more sophisticated numerical treatment of aggregates is offered in Perrine et al. (2011), but the authors themselves state the need for improvement while investigating both the adhesive threshold and the work done during internal fracture. In this work implications for the size distribution of Saturn's rings will be discussed. Unless otherwise indicated size refers to the radius of an object.

First of all, in Chapter 2, an introduction is given on applying kinetic theory to the ring system. This brief description of kinetics shows which velocity-mass range is of interest in this study: the fragmentation boundary. Second, the analytic theory and some preliminary results for fragmentation are presented in Chapter 3. In Chapter 4 the results obtained with the pure analytic theory are compared to numerically created aggregates of various types such as regular packings (Sec. 4.1), Ballistic Particle Cluster Aggregates (BPCA), and modified BPCA. First, an algorithm was created to generate the usual BPCA, followed by irregular packings based upon BPCA. Many aggregates were generated for each case with different seeds. In a next step, constituent size distributions were considered in order to model more realistic loose arrangements of planetary ring aggregates (Sec. 4.2). In Chapter 5, estimates for the collisional velocities required to break up the aggregates are given, pointing back to the work of Albers and Spahn (2006). Finally, implications for the size distribution of ring particles will be discussed in the Chapter 6.

1. INTRODUCTION

Chapter 2

Kinetic description of Saturn's rings

In Chapter 1 the importance of the coagulation and fragmentation processes for Saturn's rings has already been mentioned. These processes are a result of collisions between the particles. Firstly, we give a brief description of collision dynamics before a general approach is presented to discuss the evolution of the particle mass and velocity distribution in the rings. Kinetic theory is usually used to quantify the evolution of the ring particles in the mass-phase space. The rings are treated as a granular system, where only binary collisions occur. A generalized kinetic concept, treating the mass- and the velocity-spectrum of a granular ensemble, has been derived by Spahn et al. (2004) under assumptions of mass- and momentum conservation of the system. All collisions result either in *i)* coagulation, *ii)* restitution or *iii)* fragmentation where the collisional outcome depends on the masses of the collision partners, their mechanical properties, and their relative velocities. Thus, the collisional outcome can be assigned to these three different domains in the space of masses and velocities of the colliding grains as sketched in Fig. 2.1. The borders between the domains (see Fig. 2.1) (coagulation, restitution and fragmentation) can be obtained by analyzing the collisions

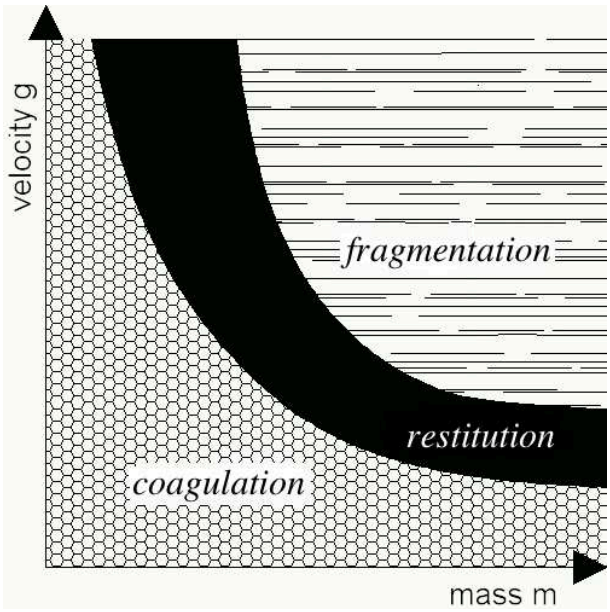

Figure 2.1: Domain diagram: the masses m (their ratio) and the relative impact speed g between colliding particles determine the result of a collision: i) coagulation, ii) restitution or iii) fragmentation.

between ring aggregates, taking into account dissipation and the internal properties of the collision partners, that is, including adhesion and self-gravity. Albers and Spahn (2006), Albers (2006) and later Brilliantov et al. (2007) studied the boundaries between coagulation and restitution for binary ice aggregates. Consequently, crucial aim of this thesis is to estimate the location of the fragmentation border for aggregates made up from many smaller adhering constituents. Before we go into the details involved in this task, we will first present the basics of the kinetic theory.

2.1 Collision dynamics

Under the consideration of icy ring particles, the collisions in the rings are inelastic and the dissipation of kinetic energy during the impact is usually measured by the

coefficient of restitution, $0 \leq \varepsilon < 1$ [3]. In the limit of $\varepsilon = 0$ all kinetic energy of the motion in the direction perpendicular to impact plane is dissipated – transformed into heat, internal deformation or formation of cracks in the bulk of the collision partner. As a result of the dissipation, an aggregate is formed while collision partners rest on top of each other, provided that the collisional constituents are finally hold together by adhesion and/or gravity. The adhesive contact is quantified by the surface energy, γ_0, and the contact area formed between the collision partners (Johnson et al., 1971). Such a sticking occurs at quite low impact speeds and alters the size distribution (towards larger sizes). The other two possible outcomes of a collision are: restitution and fragmentation, depending on the relative velocities and masses of the collision partners, and their mechanical properties. The restitution leaves the quantity $n(m,\mathbf{r})$ unchanged and only the velocity distribution $f(\mathbf{r},\mathbf{v};m)$ is modified. In the cases of coagulation (sticking) and fragmentation the size distribution $n(m,\mathbf{r})$ and the velocity spectrum $f(\mathbf{r},\mathbf{v};m)$ are both altered. For a common kinetic description it is advantageous to introduce a generalized distribution function $F(m,\mathbf{r},\mathbf{v}) = n(m,\mathbf{r})f(\mathbf{r},\mathbf{v};m)$ as described below (the time t is dropped in the argument list for brevity). In this Section we want to sketch the collision dynamics for the *ii)* restitutive case which distinguishes between the two collisional results: *i)* coagulation, and *iii)* fragmentation – both are described at the end of this kinetics chapter. Prior to collision the relative velocity between both collision partners is defined by

$$\mathbf{g} = \mathbf{v}_1 - \mathbf{v} \,, \tag{2.1}$$

where $\mathbf{v}$ and $\mathbf{v}_1$ are their velocities.

[3] Here the simplest case of collisional dynamics is briefly described which only considers translational degrees of freedom and ε is to the normal coefficient of restitution. For the case of $\varepsilon = 1$, the total kinetic energy is conserved i.e the collision occurs elastically – but this case is not relevant for planetary rings.

Their common center of mass moves at a constant velocity

$$\mathbf{v}_s = \frac{(m\mathbf{v} + m_1\mathbf{v}_1)}{(m+m_1)} \quad , \tag{2.2}$$

where $m_{(i)}$ denotes the particle masses. Due to the conservation of total momentum, the collision cannot change the center of mass motion, but the relative velocities before and after the collision are modified – see Fig. 2.2. A collision takes place in a plane defined by the vector $\mathbf{g}$ and the unit vector $\mathbf{k}$ pointing from the center of the collision

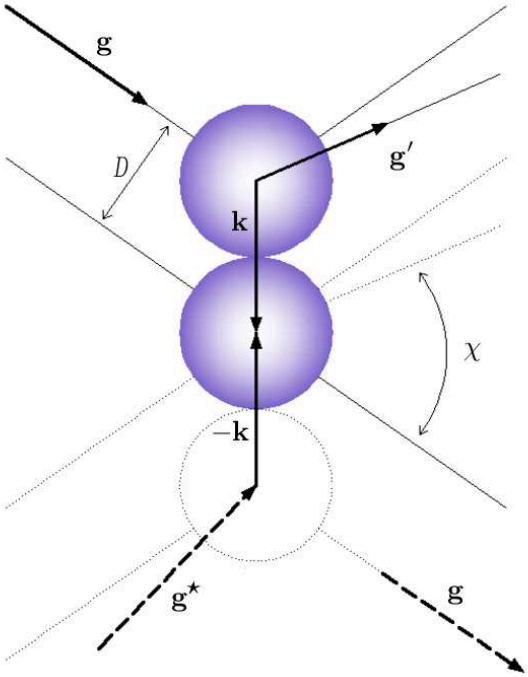

Figure 2.2: Inelastic collision of two particles. This figure shows the geometrical relations of velocities involved during collision, only translational degrees of freedom are considered. $\mathbf{g}$ and $\mathbf{g}'$ are the relative velocities before and after impact, respectively, where solid vectors denote the forward ($+t$) and dashed ones the time reversed collision ($t \to -t$). The magnitude of the normal component $\mathbf{g}' \cdot \mathbf{k}$ of the relative velocity after impact is reduced by a factor ε, the coefficient of normal restitution. In case of the time reversed collision, the magnitude of the normal component $\mathbf{g}^* \cdot \mathbf{k}^*$ before the impact has to be larger by a factor $1/\varepsilon$.

partner centered at $\mathbf{r}_1$ to the center of the particle under consideration at $\mathbf{r}$ according to $\mathbf{k} = (\mathbf{r}-\mathbf{r}_1)/|\mathbf{r}-\mathbf{r}_1|$. Given this, the normal component of the relative velocity $(\mathbf{g}\cdot\mathbf{k})$ will be reduced due to the dissipation occurring in a binary collision as follows

$$\mathbf{g}'\cdot\mathbf{k} = -\varepsilon\,\mathbf{g}\cdot\mathbf{k} \ , \tag{2.3}$$

with the post-collisional relative velocity $\mathbf{g}'$ (see Fig. 2.2). The particle velocities $\mathbf{v}$ and $\mathbf{v}_1$ (before and after collision $\mathbf{v}'$ and $\mathbf{v}_1'$) can be written in terms of $\mathbf{v}_s$ and $\mathbf{g}$ using Eqs. (2.1) - (2.2) to give

$$\mathbf{v} = \mathbf{v}_s - \frac{m_1}{m+m_1}\mathbf{g} \tag{2.4}$$

$$\mathbf{v}_1 = \mathbf{v}_s + \frac{m}{m+m_1}\mathbf{g}. \tag{2.5}$$

Thus, the collisional changes of the relative - and the center of mass velocities under consideration read finally

$$\mathbf{v}_s = \mathbf{v}_s' \ , \tag{2.6}$$

and combining Eqs. (2.1) - (2.6) we finally arrive at the post-collisional velocities of both collision partners

$$\mathbf{v}' = \mathbf{v} + \frac{m_1}{m+m_1}(1+\varepsilon)(\mathbf{g}\cdot\mathbf{k})\mathbf{k} \tag{2.7}$$

$$\mathbf{v}_1' = \mathbf{v}_1 - \frac{m}{m+m_1}(1+\varepsilon)(\mathbf{g}\cdot\mathbf{k})\mathbf{k} \ . \tag{2.8}$$

2.2 Kinetics

The evolution of a granular gas can be described using the kinetic equations including the influence of the external forces, **f**, and interactions between the ring particles, i.e. direct (contact) collisions and gravitational interactions. First we quantify the number of particles dN in the phase space volume element $\mathrm{d}^3\mathbf{V}\,\mathrm{d}^3\mathbf{R}\,\mathrm{d}M$ by defining the generalized distribution function $F(M,\mathbf{R},\mathbf{V},t)$ (DF) via the equation

$$\mathrm{d}N = F(M,\mathbf{R},\mathbf{V},t)\,\mathrm{d}^3\mathbf{R}\,\mathrm{d}^3\mathbf{V}\,\mathrm{d}M\ , \tag{2.9}$$

where M denotes the particle mass, **R**, the location vector, **V**, the velocity vector, and the time t. In general, the time evolution of the distribution function can be written as

$$\frac{\mathrm{D}}{\mathrm{D}t}F(M,\mathbf{R},\mathbf{V},t) = \left.\frac{\mathrm{D}F}{\mathrm{D}t}\right|^{(c)} + \left.\frac{\mathrm{D}F}{\mathrm{D}t}\right|^{(r)} + \left.\frac{\mathrm{D}F}{\mathrm{D}t}\right|^{(f)}\ , \tag{2.10}$$

with the right hand sides being the collisional changes of the distribution function. The superscripts of the three terms refer to the three collisional outcomes: coagulation (c), restitution (r), and fragmentation (f). The substantial derivative is defined by $\frac{\mathrm{D}}{\mathrm{D}t} = \frac{\partial}{\partial t} + \mathbf{V}\cdot\frac{\partial}{\partial\mathbf{R}} + \frac{\mathbf{f}}{m}\cdot\frac{\partial}{\partial\mathbf{V}}$. This change Eq. (2.10) with time, $\frac{\mathrm{D}F}{\mathrm{D}t}$, is dominated by gain ($\mathcal{G}$) and loss terms ($\mathcal{L}$) in the combined mass-phase-space,

$$\frac{\mathrm{D}}{\mathrm{D}t}F = \mathcal{G}^{(i)} - \mathcal{L}^{(i)}\ , \tag{2.11}$$

which are caused by the particle's (aggregate's) collisions. The gain $\mathcal{G}$ measures the number (rate) of particles which are deflected into the phase space volume $\mathrm{d}^3\mathbf{V}\,\mathrm{d}^3\mathbf{R}\,\mathrm{d}M$ during the (negligibly short) time interval δt (collisional duration). Accordingly, $\mathcal{L}$ denotes the loss rate of particles out of that volume element in the same time interval.

In the following we briefly sketch the values characterizing the gain and the loss terms. Both rates are proportional to the two-particle distribution function

$$F^{(2)}(m,\mathbf{r},\mathbf{v};m_1,\mathbf{r},\mathbf{v}_1,t)\ ,$$

being the probability to simultaneously find two particles at the same location $\mathbf{r}$. The fact that only $\mathbf{r}$ (one space vector instead of $\mathbf{r}$ and $\mathbf{r}_1$) appear in the list of arguments means that finite sizes of the aggregates are neglected (collision occurs at a point $\mathbf{r}$ in space). Furthermore, apart from the moment of the collision (which is considered to be infinitesimally short) we assume that the aggregates are uncorrelated – called molecular chaos assumption. With these assumptions the two-particle distribution can simply be factorized

$$F^{(2)}(m,\mathbf{r},\mathbf{v},t;\ m_1,\mathbf{r}_1,\mathbf{v}_1,t) = F(m,\mathbf{r},\mathbf{v},t)\cdot F_1(m_1,\mathbf{r}_1,\mathbf{v}_1,t). \tag{2.12}$$

Using the relative $\mathbf{g}$ and the center of mass velocities $\mathbf{v}_s$, respectively, the gain and loss terms for particles/aggregates, obeying the phase-space values $M,\mathbf{R},\mathbf{V}$, can be written as (Spahn et al., 2004)

$$\begin{aligned}\mathcal{G}^{(i)}(M,\mathbf{R},\mathbf{V},t) &= \int_0^\infty \mathrm{d}m \int_0^\infty \mathrm{d}m_1 \\ &\int_{\mathbf{R}^3} \mathrm{d}^3\mathbf{v}_s \int_{\mathcal{D}_i} \mathrm{d}^3\mathbf{g}\, W_{\mathcal{G}}^{(i)}(M,\mathbf{V};m,m_1,\mathbf{g})\, F(m,\mathbf{v})\, F_1(m_1,\mathbf{v}_1),\end{aligned} \tag{2.13}$$

$$\begin{aligned}\mathcal{L}^{(i)}(m,\mathbf{R},\mathbf{V},t) &= \int_0^\infty \mathrm{d}m \int_0^\infty \mathrm{d}m_1 \\ &\int_{\mathbf{R}^3} \mathrm{d}^3\mathbf{v}_s \int_{\mathcal{D}_i} \mathrm{d}^3\mathbf{g}\, W_{\mathcal{L}}^{(c/f)}(M,\mathbf{V};m,m_1,\mathbf{g})\, F(m,\mathbf{v})\, F_1(m_1,\mathbf{v}_1)\ .\end{aligned} \tag{2.14}$$

The distribution functions F and F_1 refer to the states prior to the collision, where $W^i_{\mathcal{G}/\mathcal{L}}$ are integration kernels which contain the collision frequency, proportional to the relative speed $|\mathbf{g}|$ of the colliding aggregates and to the cross-section $\sigma_{cross} = (R+R_1)^2/4 \propto (m^{1/3}+m_1^{1/3})^2$ (approximation for hard spheres). The conservation of mass and momentum enter the kernels via delta function. Altogether, the integral kernels $W^i_{\mathcal{G}/\mathcal{L}}$ measure the transition probability of a collisional outcome (masses M and velocities $\mathbf{V}$) for given pre-collisional state: masses m, m_1 and relative speed $\mathbf{g}$, in cases of coagulation and fragmentation (indicated by the indices $\mathcal{G}/\mathcal{L}$). In cases, when long-ranged forces become important – i.e. Coulomb forces, gravity – a "focusing" factor $\mathcal{F}$ enters the kernels, containing *e.g.*, the charge of grains, their masses (Safronov factor, gravitational focusing), or other particle properties which can alter the cross-section $\sigma_{cross} \propto (R+R_1)^2$. The integration domains of coagulation, fragmentation (or restitution) are labeled by $\mathcal{D}_i$ which depend on the masses of the colliding particles m, m_1 and their relative speed g – i.e. on the collision dynamics. For example, coagulation and fragmentation occur for impact speeds of $0 < g < g_c(m, m_1)$ and $g_f(m, m_1) < g < \infty$, respectively (see Fig. 2.1), meaning low velocity collisions make coagulation/sticking quite likely; in contrast: violent, high impact speeds can destroy the collision partners. In the next Subsections, we shall discuss the kernels of the three different collision regimes/domains. Firstly, we focus on restitutive collisions, which deviates somewhat from the other two cases, which will be addressed finally.

2.2.1 Restitution

In case of restitutive collisions between two particles with masses m and m_1 the mass distribution $n(m, \mathbf{r})$ is not affected, because both colliding partners remain intact. Instead, both grains experience an exchange in momentum while dissipating mechanical

energy in partly inelastic collisions. We factorize the generalized distribution function as

$$F(m,\mathbf{r},\mathbf{v}) = n(m,\mathbf{r})\, f(\mathbf{r},\mathbf{v};m) \ , \tag{2.15}$$

pointing to an independence of the mass (size) spectrum from the velocity dispersion.

The latter depends on the phase-space state variables $(\mathbf{r},\mathbf{v})$ – the mass m can parametrically enter the distribution function, indicated in the argument list (for brevity we dropped the time t from the arguments). As a simple example, in equilibrium of a ideal gas mixture of different (distinct masses) molecules/particles a common temperature T exists but the thermal fluctuating speeds depend on their masses according to energy equi-partition as $\langle \Delta \mathbf{v}^2 \rangle \propto T/m$ which is a parameter of the velocity distribution function. Normalizations and the zeroth moment define the particle number density of a certain species m as $n(m,\mathbf{r}) = \int \mathrm{d}^3\mathbf{v}\, F$ meaning $\int \mathrm{d}^3 f = 1$. The particle number density of the whole ensemble is given by $n(\mathbf{r}) = \int \mathrm{d}m\, n(m,\mathbf{r})$. Next, in order to write the collisional integral in terms of gain and loss, specifying the probability of a particle being scattered in or out of the velocity volume element ($\mathrm{d}^3\mathbf{v}$ around $\mathbf{v}$), one has to consider the initial velocities of the impact partner. These pre-collisional velocities are denoted by $\mathbf{v}^\star$ and $\mathbf{v}_1^\star$ in the gain term before they are scattered into the considered velocity volume element. It is known that the inelasticity of the collision causes a symmetry-breaking due to the "loss" of mechanical kinetic energy, therefore the pre-collisional velocity, $\mathbf{g}^\star = \mathbf{v}_1^\star - \mathbf{v}^\star$, is not equal to the final velocity, $\mathbf{g}'$, of a conservative collision. Thus, the pre-collisional normal component changes in accordance with

$$\begin{aligned} \mathbf{g}^\star \cdot \mathbf{k}^\star &= -\varepsilon^{-1}\, \mathbf{g}\cdot\mathbf{k} \\ \mathbf{g}^\star \cdot \mathbf{k} &= \varepsilon^{-1}\, \mathbf{g}\cdot\mathbf{k}\,, \end{aligned} \tag{2.16}$$

with $\mathbf{k}^\star = -\mathbf{k}$. In accordance with the Eqs. (2.6) - (2.8) and using $\mathbf{v}_s = \mathbf{v}_s^\star$, the pre-collisional velocities in the gain term can be written

$$\mathbf{v}^\star = \mathbf{v} + \frac{m_1}{m+m_1}(1+\varepsilon^{-1})(\mathbf{g}\cdot\mathbf{k})\mathbf{k} \tag{2.17}$$

$$\mathbf{v}_1^\star = \mathbf{v}_1 - \frac{m}{m+m_1}(1+\varepsilon^{-1})(\mathbf{g}\cdot\mathbf{k})\mathbf{k}\ . \tag{2.18}$$

The so-called *Stosszahl-Ansatz* introduced by Boltzmann, which means counting the number of particles scattered in and out of the considered velocity-volume element $\mathrm{d}^3\mathbf{v}$ around $\mathbf{v}$, directly leads to kinetic equation for the restitutive case (see for instance: Goldreich and Tremaine, 1978):

$$\begin{aligned}\frac{\mathrm{D}F^{(r)}}{\mathrm{D}t} &= n(M,\mathbf{r},t)\int\limits_{\mathcal{D}_\mathcal{R}} \mathrm{d}m_1\, n(m_1,\mathbf{r},t)\int\limits_{\mathcal{D}_\mathcal{R}} \mathrm{d}^3\mathbf{v}_1\,\mathrm{d}^2\mathbf{k}\,\sigma_{cross}\,\Theta(\mathbf{g}\cdot\mathbf{k})[\mathbf{g}\cdot\mathbf{k}]\times \\ &\times \left\{\frac{f(M,\mathbf{v}^\star,t)\,f(m_1,\mathbf{v}_1^\star,t)}{\varepsilon^2} - f(M,\mathbf{v},t)\,f(m_1,\mathbf{v}_1,t)\right\} \\ &= \mathcal{G}^{(r)} - \mathcal{L}^{(r)}\end{aligned} \tag{2.19}$$

The integrals have to be taken over the restituting domain in the masses and velocity space indicated by the label $\mathcal{D}_\mathcal{R}$. The Heaviside function $\Theta(\mathbf{g}\cdot\mathbf{k})$ ensures that only approaching particles that are going to collide are taken into account. The coefficient ε^{-2} in the gain term accounts for the shrinking of the phase space due to dissipation (violation of the Liouville theorem – phase space is not constant).

To improve understanding, we can consider that the form of the kernel $\sigma_{cross}(\mathbf{g}\cdot\mathbf{k})n(m)f(\mathbf{v})n(m_1)f(\mathbf{v}_1)$ can be interpreted as a projectile flux $(\mathbf{g}\cdot\mathbf{k})n(m_1)f(\mathbf{v}_1)$ approaching a target with cross-section σ_{cross}. This sets the number of collision per unit time in the cylinder volume (see Fig. 2.3). This collision frequency is weighted by the number of targets $n(m)f(\mathbf{v})$ which enter the volume (per unit time).This collision

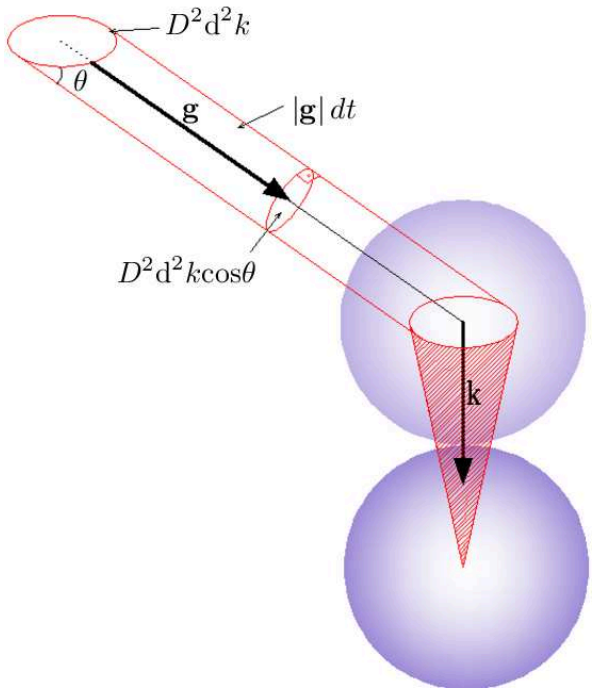

Figure 2.3: Collision of two particles of diameter D.

rate has to be summed over all velocities and solid angles $\mathrm{d}^2\mathbf{k}$, giving the integro-differential equation (2.20).

For a mono disperse ensemble, $n(m_1, \mathbf{r}, t) = \delta(m_1 - M)\, n(\mathbf{r}, t)$, one ends up with the usual Boltzmann kinetic equation for granular gases.

2.2.2 Coagulation and Fragmentation

Fragmentation and coagulation of ring particles are the alternative outcomes of collisions, modifying the resulting size distribution $n(M, \mathbf{r})$ of the ring particles. Using the equations (2.13) and (2.14) the fragmentation and coagulation integration kernels can

be written as (Spahn et al., 2004)

$$W^{(c)}_{\mathcal{G}/\mathcal{L}} = \sigma_{cross}\,|\mathbf{g}|\;\mathcal{F}\;\delta(m_{\mathcal{G}/\mathcal{L}} - M)\;\delta\left(\mathbf{v}_{\mathcal{G}/\mathcal{L}} - \mathbf{V}\right), \tag{2.20}$$

$$W^{(f)}_{\mathcal{G}} - W^{(f)}_{\mathcal{L}} = W^{(f)} = \sigma_{cross}\,|\mathbf{g}|\;\mathcal{F}\;[\mathcal{P}(M,\mathbf{V}|m,m_1,\mathbf{g}) - \delta(m_1 - M)\delta(\mathbf{v}_1 - \mathbf{V})], \tag{2.21}$$

where $m_{\mathcal{G}} = m + m_1$ and $m_{\mathcal{L}} = m_1$, and $\mathbf{v}_{\mathcal{G}} = (m\mathbf{v} + m_1\mathbf{v}_1)/(m + m_1)$ and $\mathbf{v}_{\mathcal{L}} = \mathbf{v}_1$. These distinctions arise from different integration paths for gain ($m + m_1 = const. = M$; two colliding particles merge into one) and loss ($m = const.$) terms in the (m, m_1) parameter space. *Dirac*'s Delta function is denoted by $\delta(x)$ and assures conservation of mass and momentum. Coagulating particles will form an aggregate with mass $M = m + m_1$ and velocity $\mathbf{v}_s$. For simplicity we assume solid spherical particles $m \propto R^3$, which then form, as a result of the collision, new solid spherical particles of a different mass, we deliberately neglect fractal growth (agglomeration) and the impact geometry.

Nevertheless, this does not change the dependencies in Eqs. (2.20) and (2.21), and can be implemented in more detailed studies accounting for generally observed growth of fractal shaped bodies (Kempf et al., 1999) in form of $m \propto R^{D_\mathrm{f}}$, where D_f denotes the fractal dimension. In the case of destructive impacts, particles are destroyed, forming post-collisional size and velocity distributions (Eq. (2.21)), e.g. $\mathcal{P}(M,\mathbf{V}|m,m_1,\mathbf{g})$, i.e. the particle number is increased. In contrast to coagulation, resulting fragments may cover a broad range of masses and velocities, which are hard to derive from basic principles, but can be found in extensive experimental studies of fragmentation. Bearing this in mind, the gain and loss term of fragmentation may be written using a normalized conditional distribution function $\mathcal{P}(M,\mathbf{V}|m,m_1,\mathbf{g})$ of the generated debris as in eq. (2.21) and as suggested in Krivov et al. (2000). Summarizing the kinetics of

coagulation and fragmentation one may write

$$\frac{\mathrm{D}}{\mathrm{D}t}F(M,\mathbf{R},\mathbf{V},t) = \int_0^\infty \mathrm{d}m \int_0^\infty \mathrm{d}m_1 \int_{\mathbf{R}^3} \mathrm{d}^3\mathbf{v}_s \left[\int_{\mathcal{D}_c} \mathrm{d}^3\mathbf{g}\left(\frac{1}{2}W_{\mathcal{G}}^{(c)} - W_{\mathcal{L}}^{(c)}\right)FF_1 + \int_{\mathcal{D}_f} \mathrm{d}^3\mathbf{g}W^{(f)}FF_1\right]. \quad (2.22)$$

Due to symmetry with respect to an exchange of particles a factor of $1/2$ appears in the coagulation gain term. This Eq. (2.22) can finally be completed by adding the rhs of Eq. (2.11) so that one arrives at a complete kinetic description of coagulation, restitution, and fragmentation. All contributions $\frac{\mathrm{D}}{\mathrm{D}t}^{(i)}F$ (with (i) standing for $(c),(f),$ and (r)) are crucial in the dynamics of planetary rings. The domains in phase space, where certain contributions $\frac{\mathrm{D}}{\mathrm{D}t}^{(i)}F$ dominate, are essentially determined by the aggregate physics and mechanics, which is the main task of this thesis.

2. KINETIC DESCRIPTION OF SATURN'S RINGS

Chapter 3

Aggregate self-energy, relations and resistivity

As presented in Chapter 1 and highlighted in Chapter 2, the dynamics involved in the planetary rings promotes the agglomeration/fragmentation of the particles. Aggregates in this environment are both collisional targets and projectiles. This situation raises the question of how far an aggregate can grow. Here, in order to address this problem, simple equations are used. The aggregate specific self-energy Q, composed of contact energy and gravitational self-energy, and its specific break-up energy $Q^\star$ are considered as an estimate for its resistivity, where details of internal stress-distribution or orbital motion are not considered. The specific self-energy Q and the specific break-up energy $Q^\star$ are calculated for different aggregate configurations. It is shown that the resistivity of an aggregate may be divided into strength- and gravity regimes with a transition at a size R_t. Furthermore, it is also shown that a critical aggregate radius size $R_{\rm crit}$ exists in which an object is more likely to be destroyed than others. Moreover, these energy values, Q and $Q^\star$, are related to the damage ratio of the aggregates.

3.1 Specific self-energy Q

The total self-energy of an aggregate is given by the sum of its self-gravity E_G and internal contact energy E_A as: $E_T = E_G + E_A$. The specific self-energy (energy per mass) of an aggregate is then given by $Q = E_T/M$, where M is its mass. The gravitational energy between two constituents reads

$$E_G^{(2)} = -\frac{Gm_1m_2}{|\vec{r}_2 - \vec{r}_1|} \tag{3.1}$$

where G denotes the gravitational constant. Thus, $E_G^{(2)}$ is equal to the amount of energy needed to physically separate two particles to infinity, since gravity is a conservative force. In contrast to gravity, the collisions of icy adhesive, viscoelastic particles are irreversible (Albers and Spahn, 2006; Brilliantov et al., 2007). The energy required to separate two particles (the energy of one "adhesive bond") contains both the mechanical (elastic) energy of particle deformation u_{elas} as well as adhesive energy u_{add} which has dissipative nature (Albers and Spahn, 2006; Brilliantov et al., 2007). Taking into account both elastic and adhesive contributions the energy of an adhesive bond reads (see Appendix A for details)

$$E_A^{(2)} = -\frac{1}{5}\gamma\pi a_{eq}^2,$$

where $a_{eq}^2 = (6\pi\gamma D s_{\text{eff}}^2)^{2/3}$ is the radius of the contact area formed between the constituents, $s_{\text{eff}} = s_1 s_2/(s_1+s_2)$ denotes the effective particle size and γ is twice the surface free energy γ_0. This equation can be re-written as

$$E_A^{(2)} = -\frac{1}{5}\left(36\pi^5\gamma^5 D^2 s_{\text{eff}}^4\right)^{1/3}. \tag{3.2}$$

The bulk material constants, Young's modulus Y and Poisson ratio ν, have been combined into a single constant $D = 3(1-\nu^2)/2Y$, implicitly assuming that all particles are made of the same material. Throughout this study we use $G = 6.67\,10^{-11}\,\mathrm{m^3 kg^{-1} s^{-2}}$ and material constants commonly used for icy particles: $\rho = 0.910 \times 10^3$ kg m^{-3}, $\gamma_0 = 0.357\,\mathrm{N\,m^{-1}}$, $Y = 7 \times 10^9$ Pa and $\nu = 0.25$ (e.g. Chokshi et al., 1993; Dominik and Tielens, 1997; Brilliantov et al., 2007). We are aware that the surface adhesion γ is currently the most uncertain value and subject of ongoing debate. We therefore use an additional, lower, estimate $\gamma_0 = 0.1\,\mathrm{N\,m^{-1}}$ (Wada et al., 2008)[4] in order to account for these uncertainties in our results. For convenience, we define $A^{(\mathrm{ij})} = (36\pi^5\gamma^5 D^2)^{1/3}/5 \approx 4.45(\gamma^5 D^2)^{1/3}$ with $[A^{(\mathrm{ij})}] = \mathrm{N\,m^{-1/3}}$. Consider an aggregate of size R made of N constituent particles of radius[5] s, therefore the total self-energy of this aggregate reads

$$E_\mathrm{T} = -\frac{G}{2}\sum_{i=1}^{N}\sum_{j=1}^{N}\frac{m_i m_j}{|\vec{r}_i - \vec{r}_j|} - \frac{A^{(\mathrm{ij})}}{2}\sum_{i=1}^{N}\sum_{j=1}^{N} C_{ij}\left(\frac{s_i s_j}{s_i + s_j}\right)^{4/3}, \tag{3.3}$$

where C_{ij} is unity if particle i and j are in contact and zero otherwise. The specific self-energy reads $Q = E_\mathrm{T}/\sum_{i=1}^{N} m_i$. The gravitational self-energy is expressed as

$$E_G = -\frac{G}{2}\int_0^R\int_0^R \frac{\rho(\vec{r})\rho(\vec{r}')}{|\vec{r} - \vec{r}'|}\,\mathrm{d}^3 r\,\mathrm{d}^3 r', \tag{3.4}$$

assuming that the individual constituents are much smaller than the actual aggregate – corresponding to a mean field representation, $\langle s\rangle \ll R$. In the limit of a homogeneous sphere one obtains $E_G = -3GM^2/(5R)$. Both self-gravity E_G and contact energy E_A do not depend only on the aggregate size but also on the internal size distribution and

[4] Recently another γ_0 value of $0.19\,\mathrm{N\,m^{-1}}$ was suggested by Gundlach et al. (2011)

[5] Aggregates made of different sizes constituents are described by a constituent size distribution $f(s)$. Samples (numerical models) of those aggregates are presented in Chapter 4. Here we treat the aggregates of monomeric constituents.

arrangement of constituents - the aggregate packing style. Bulk and surface properties of an aggregate generally differ and the total self-energy, equivalent to Eq. (3.3), may be written as $E_{\mathrm{T}} = E_{\mathrm{G}}^{(\mathrm{bulk})} + E_{\mathrm{A}}^{(\mathrm{bulk})} - E_{\mathrm{surface}}$. In the limit of large aggregates $R \to \infty$, we have $E_{\mathrm{A}}^{(\mathrm{bulk})}/M \to$ constant, $E_{\mathrm{G}}^{(\mathrm{bulk})}/M \to \infty$, and $E_{\mathrm{surface}}/M \to 0$, thus the surface contribution in the total energy of the body decreases with the size. We will discuss this in more depth in Chapter 4. We further define the global filling factor of an aggregate as the ratio of total constituent volume and aggregate volume: $f = \sum_i s_i^3/R^3$. In the case of regular, crystal-like packings as the face-centered cubic (fcc), these energies may be expressed using the bulk specifications of the particular crystal structure listed in Table 3.1. In particular, the total number of contacts C and total number of particles

Table 3.1: Regular packing characteristics of single unit cell: number of constituents $\hat{N}$, bulk coordination number C_N, bulk filling factor f, and volume scaling factor $\hat{v}$ where the volume of the unit cell is $\hat{V} = \hat{v}s^3$ and s is the constituent size (check Fig. 4.2).

Packing	$\hat{N}$	C_N	$\hat{v}$	f
fcc	4	12	$16\sqrt{2}$	0.74
bcc	2	8	$\frac{64}{9}\sqrt{3}$	0.68

N of equal radius size s_0 can be directly calculated from the bulk coordination number C_{N} (number of contacts of a single constituent) as $C = NC_{\mathrm{N}}/2$ and $N = N_{\mathrm{u}}\hat{N}$ where N_{u} is the number of unit cells and $\hat{N}$ the number of constituents in a single unit cell. Further, the number of unit cells is $N_{\mathrm{u}} = 4\pi R^3/(3\hat{V})$ where $\hat{V} = \hat{v}s_0^3$ is the volume of a unit cell. The filling factor f then reduces to $f = (4\pi/3)(\hat{N}/\hat{v})$ and the aggregate mass can be written as $M = 4\pi\rho f R^3/3$. Hence, the total contact energy is the sum over all binary contacts given by Eq. (3.2) and reads

$$E_A = -A\,C_{\mathrm{N}}\,f\,R^3\,s_0^{-5/3}\,. \tag{3.5}$$

where $A = A^{(\mathrm{ij})}/(4 \cdot 2^{1/3})$. This equation is valid for any aggregate made of equal-sized spheres. Using Table 3.1 we obtain for fcc packings $E_{\mathrm{A}}^{(\mathrm{fcc})} \approx 8.8 A R^3 s_0^{-5/3}$. Similarly, $E_{\mathrm{A}}^{(\mathrm{bcc})} \approx 0.6 E_{\mathrm{A}}^{(\mathrm{fcc})}$. We combine Eqs (3.4) and (3.5) and write the total specific self-energy

$$Q \;=\; Q_G + Q_A = -\frac{4\pi}{5} G\rho f R^2 - \frac{3}{4\pi}\frac{A C_{\mathrm{N}}}{\rho} s_0^{-5/3}, \tag{3.6}$$

which depends on average properties such as filling factor, coordination number, and constituent size. As expected from a short range interaction, Q_{A} is independent of the actual aggregate size. Fig. 3.1 shows the specific self-energy in Eq. (3.6) for fcc aggregates as a function of radius R. Different horizontal lines correspond to different sizes of the monomer constituents, or different γ values.

Regular packed aggregates typically show high self-energies due to their dense packing (high interconnectivity) resulting in both larger gravitational and adhesive contributions. In general, the self-energy is primarily determined by the internal arrangement or packing style, parameterized by the average coordination number and filling factor. As seen in Fig. 3.1 the specific self-energy can be divided into a strength-dominated and gravity-dominated regime with a transition occurring at size R_{t} where $Q_{\mathrm{A}}(R_{\mathrm{t}}) = Q_{\mathrm{G}}(R_{\mathrm{t}})$. Solving this equation yields

$$R_{\mathrm{t}}^2 = \frac{15}{16\pi^2}\frac{A}{G}\frac{C_N}{\rho^2 f} s_0^{-5/3}. \tag{3.7}$$

An aggregate made of icy cm-sized fcc-arranged particles has R_{t} between 1 and 5 m (cf. Fig. 3.1(b)). Similar to Q, the transition size R_{t} primarily depends on constituent size and adhesive strength. Generally, stronger adhesion and smaller constituent sizes yield larger transition sizes. Objects larger in size than R_{t} lie in the gravity regime,

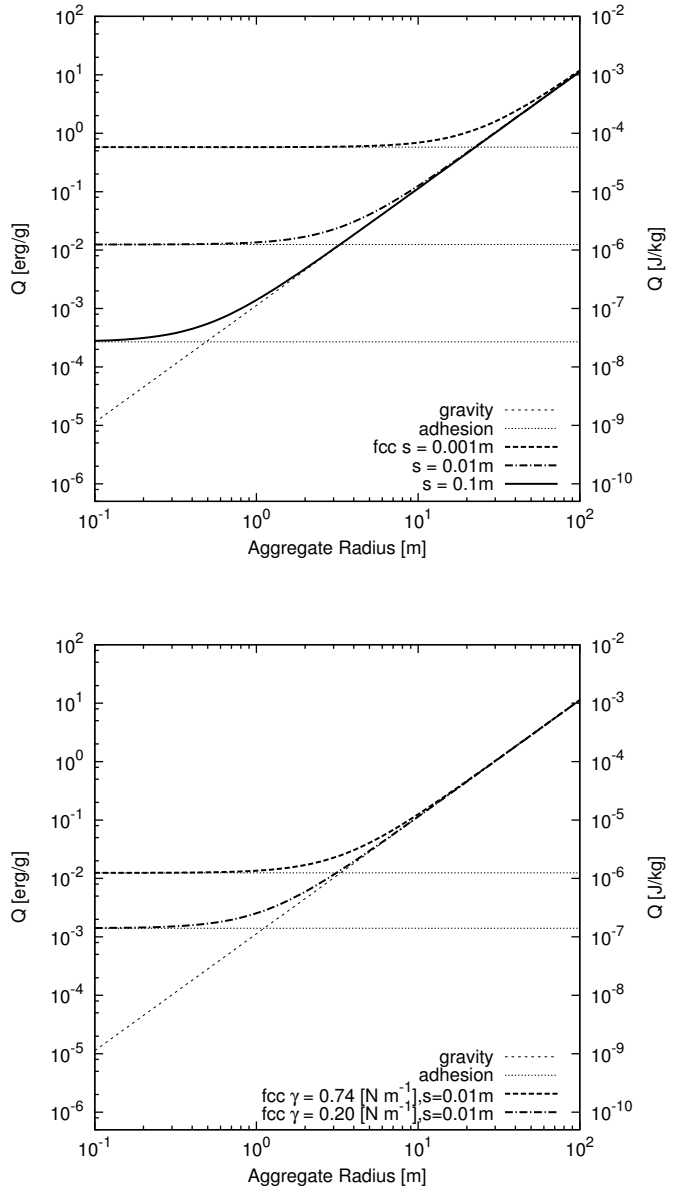

Figure 3.1: The specific self-energy for fcc aggregates ($C_N = 12$, $f = 0.74$) using Eq. (3.6) for (a) various constituent sizes s_0 and (b) different adhesion strengths. The transition from strength-dominated to gravity-dominated self-energy occurs at the intersection of the gravity and adhesion lines – at transition radius R_t.

and their own gravitational field is sufficient to hold them together. Aggregates smaller then R_t are dominated by their internal strength from adhesive bonds and so they are in the strength regime. This division into a strength-dominated and gravity-dominated

regime directly translates to an aggregate resistivity and there are implications for the probability of fragmenting an aggregate, which will be discussed in the next section.

3.2 Specific break-up energy $Q^\star$

The previous derivations show that energy must be provided in order to break an aggregate, to create new surfaces, or – at least – to rearrange individual constituents. Impacts of external objects or between the aggregates and tidal stresses due to the nearby planet are the sources of energy required to these processes (see discussion in Chapter 5). Any configurational changes of the aggregate leads to changes in the effective contact surface, including broken bonds and newly created surfaces. As these processes are generally irreversible, a fraction of this impact energy will inevitably be dissipated in the form of heat. Total energy is conserved and

$$\sum_i E_{\text{fragment}} = E_{\text{T}} + W_A + W_G + \text{generated heat}\,, \tag{3.8}$$

where W_A denotes the work done to create new surfaces and W_G is the work done to physically separate the fragments within their own mutual gravitational field, and E_{fragment} and E_{T} are the respective self-energies. In the following we will assume a final fragmentation outcome and disregard dissipative processes (meaning that all processes are adiabatically slow). For the sake of simplicity, we concentrate on impacts that fragment the aggregate and exclude reconfiguration. Also, we concentrate on the energy necessary to split an aggregate and neglect any kinetic energy that fragments might have (fragments are considered to be at rest). Further, since our main goal is to estimate the effects of collisions within planetary rings, which are typically low-velocity collisions, no shock wave generation during impacts is taken into account

(quasi-static approximation). We then obtain the expression

$$Q^{\star}(R) \;=\; \frac{W_{\rm A}(R)+W_{\rm G}(R)}{M}. \tag{3.9}$$

In the literature, the specific energy required to break-up is typically referred as $Q^{\star}$ and is defined as the threshold energy required to break an object so that the largest fragment remaining is half the mass of the original target object (e.g. Love and Ahrens, 1996; Krivov et al., 2005). We approximate $W_{\rm G}$ by the gravitational self-energy as given in Eq. (3.4) and estimate that this approach is accurate to within 10%. In order to estimate the work $W_{\rm A}$ required to create a new surface area S we define an average adhesion energy density as

$$\bar{\gamma} \;=\; \frac{E_{\rm A}}{V}. \tag{3.10}$$

In the bulk of a regular packed aggregate of radius R with monomers of size s_0 it reads

$$\bar{\gamma} \;=\; -\frac{3}{4\pi} A C_{\rm N} f s_0^{-5/3}. \tag{3.11}$$

Breaking the aggregate by simply disconnecting existing bonds along will form a rupture surface with the average thickness as wide as the radius of an individual constituent s_0. Thus, $W_{\rm A} = \bar{\gamma} S s_0$. In agreement with the literature we let the largest fragment contain half of the mass of the original aggregate. In one of the extreme cases this will create *two* equal-sized fragments and two new surfaces with area of $S_{\rm min} = \pi R^2$ corresponding to a minimum work required $W_{\rm A}^{\rm min}$, equivalent to "splitting the aggregate in *halves*".

In reality, however, the actual crack surface has variable roughness and is enlarged due

to the arrangement of individual constituents. Depending on the energy input, multiple rupture lines may occur that allow for the creation of multiple fragments. The newly created surface area can then be calculated using a fragment size distribution $f(\tilde{R})$ as

$$S = \int_{\tilde{R}_{\min}}^{\tilde{R}_{\max}} \pi \tilde{R}^2 f(\tilde{R}) \, \mathrm{d}\tilde{R}. \tag{3.12}$$

Without loss of generality, we assume that fragments are distributed according to a power-law $f(\tilde{R}) = \alpha \tilde{R}^{-p}$; the numerical constant α may be obtained from mass conservation (i.e. here conservation of volume) to give $R^3 = \int_{\tilde{R}_{\min}}^{\tilde{R}_{\max}} \alpha \tilde{R}^{3-p} \mathrm{d}\tilde{R}$. Then, by simple relation $W_\mathrm{A}/S = W_\mathrm{A}^{\min}/S_{\min}$ and Eq. (3.12) the required work to create multiple fragments is calculated as

$$W_\mathrm{A} = W_\mathrm{A}^{\min} R \, \mathcal{F}\left(p, \tilde{R}_{\min}, \tilde{R}_{\max}\right), \tag{3.13}$$

where

$$\mathcal{F}\left(p \notin [3,4], \tilde{R}_{\min}, \tilde{R}_{\max}\right) = \frac{4-p}{3-p} \frac{(\tilde{R}_{\max}^{3-p} - \tilde{R}_{\min}^{3-p})}{(\tilde{R}_{\max}^{4-p} - \tilde{R}_{\min}^{4-p})}, \tag{3.14}$$

$$\mathcal{F}\left(p = 3, \tilde{R}_{\min}, \tilde{R}_{\max}\right) = \frac{1}{\tilde{R}_{\max} - \tilde{R}_{\min}} \log\left[\frac{\tilde{R}_{\max}}{\tilde{R}_{\min}}\right], \tag{3.15}$$

$$\mathcal{F}\left(p = 4, \tilde{R}_{\min}, \tilde{R}_{\max}\right) = \left(\frac{1}{\tilde{R}_{\min}} - \frac{1}{\tilde{R}_{\max}}\right) \left(\log\left[\frac{\tilde{R}_{\max}}{\tilde{R}_{\min}}\right]\right)^{-1}. \tag{3.16}$$

Finally, we obtain

$$Q^\star(R; p, \tilde{R}_{\min}, \tilde{R}_{\max}) = -\frac{3}{5}\frac{GM}{R} + W_\mathrm{A}^{\min} \frac{R}{M} \mathcal{F}\left(p, \tilde{R}_{\min}, \tilde{R}_{\max}\right). \tag{3.17}$$

We fix the size (radius) of the largest fragment $\tilde{R}_{\max}$ to correspond to half of the aggregate mass (e.g. Love and Ahrens, 1996) and further assume that the largest fragment

has the internal density of the aggregate ρ_{agg}. Then, $\tilde{R}_{max} = R/\sqrt[3]{2}$. The smallest possible fragment size $\tilde{R}_{min}$ is equal to the size of the smallest constituent, in this case $\tilde{R}_{min} = s_0$. Equation (3.17) can then be written as

$$Q^\star(p, s_0, R) = -\frac{4\pi}{5} G\rho f R^2 - \frac{9}{16\pi}\frac{AC_N}{\rho} s_0^{-2/3} \mathcal{F}\left(p, s_0, R/\sqrt[3]{2}\right). \quad (3.18)$$

In the case of splitting the aggregates in half we may write

$$Q^\star(\text{halves}) = -\alpha_G R^2 - \alpha_A R^{-1} \quad (3.19)$$

$$\alpha_G = \frac{4\pi}{5} G\rho f \quad (3.20)$$

$$\alpha_A = \frac{9}{16\pi}\frac{AC_N}{\rho} s_0^{-2/3} \quad (3.21)$$

where $[\alpha_G] = \mathrm{s}^{-2}$ and $[\alpha_A] = \mathrm{J\,m\,kg}^{-1}$. Figure 3.2(a) shows results for various fragment size distribution slopes using Eq. (3.18) for fcc aggregates. Following Love and Ahrens (1996) specific impact energies above $Q^\star_{min}$ typically yield more numerous and smaller fragments; lower specific energies only cause cratering and spallation but leave the target essentially intact. Naturally, the upper limit for $Q^\star$ is Q, the total self-energy of an aggregate, resulting in the total disruption of the aggregate. For cases populating the area between the limiting curves $Q^\star$ and Q less than 50% of the original bonds are left intact. The related damage ratios (D_R), defined in Moreno-Atanasio and Ghadiri (2006) as the ratio of broken contacts to the initial number of contacts, are shown in Fig. 3.2(b). Comparing Fig. 3.2(a) and 3.2(b) it is revealed, as expected that, with higher damage ratios the number of fragments increase. With 100% damage done the aggregate is completely destroyed as $Q^\star = Q$. Moreover, Fig. 3.2(a) suggests that aggregates of a certain critical size R_{crit} are more vulnerable to being damaged than others. At this R_{crit} the energy required to break-up $Q^\star$ assumes a global minimum

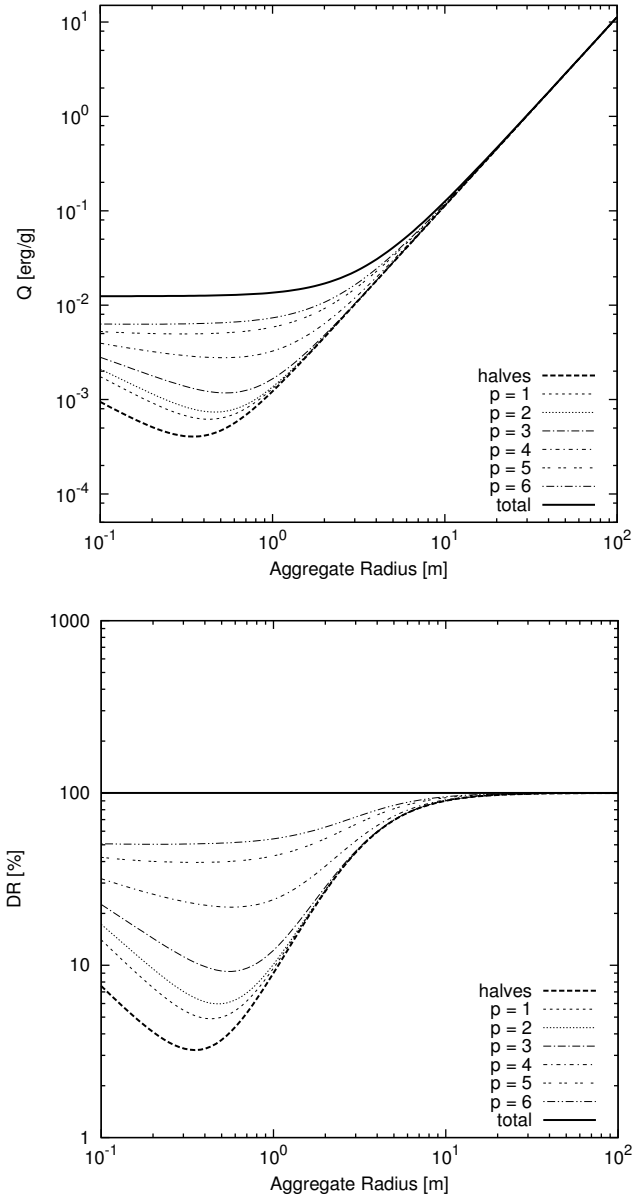

Figure 3.2: Different input energies lead to different fragmentation outcomes ranging from two fragment *halves* (each with half the mass) to *total* disruption ($Q^\star = Q$): (a) Eq. (3.18) is computed using $s_0 = 1\,\mathrm{cm}$, (b) related damage ratios in percent of broken contacts (Moreno-Atanasio and Ghadiri, 2006).

(see Fig. 3.3), and one can conclude that this is the size where aggregates are most

likely to be destroyed, so we infer from Eq. (3.18)

$$R_{\rm crit}^3 = \frac{\alpha_{\rm A}}{2\alpha_{\rm G}} = \frac{3}{8}\, s_0 R_{\rm t}^2 \,. \tag{3.22}$$

In Figure (3.3) we illustrate the critical and threshold radius for fcc aggregates with $s_0 = 1\,\mathrm{cm}$. Average bulk properties of aggregates may be used together with the mean-

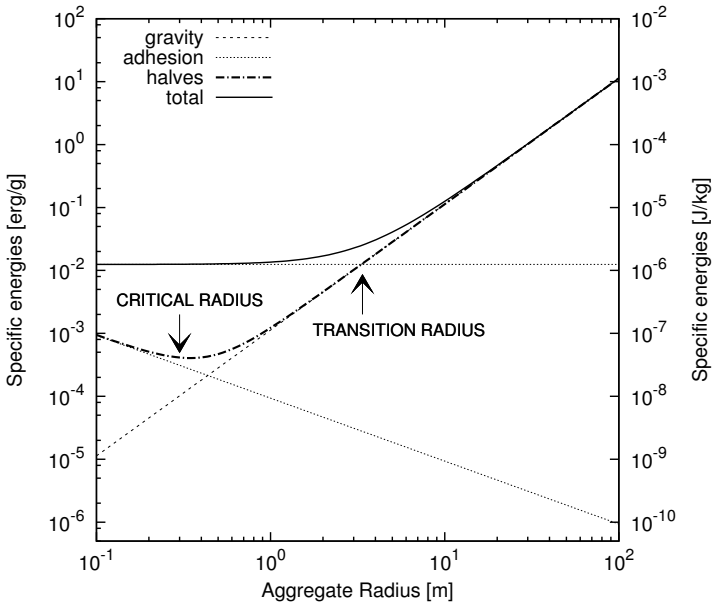

Figure 3.3: Specific energies for fcc aggregates with particle sizes $s_0 = 1\,\mathrm{cm}$ The *total* energy Q given by Eq. (3.6) is the sum of the specific adhesive and gravitational self-energies and correspond to the horizontal line. In order to break an aggregate into two equal-sized *halves* we calculate the minimum specific energy $Q^\star$ using Eq. (3.18) - the downwards sloping line. We mark the location of transition $R_{\rm t}$ and critical radius $R_{\rm crit}$. The first marks the transition between the strength-dominated and gravity-dominated regime. The latter marks which aggregate size is most vulnerable to destruction and is defined as the global minimum of $Q^\star(R)$. Even if the case of break an aggregate into two halves can be considered artificial and may not really reflect the rupture of aggregate like bodies, this approach is in qualitative agreement with Love and Ahrens (e.g. 1996).

field equations Eqs. (3.7) and (3.22) to calculate the expected transition and critical radii for various packing styles. Figure 3.4 shows the results in function of constituent size. The border of the gray-shaded area marks the minimum size of an aggregate,

taken to be the characteristic radius of an aggregate consisting of two constituents particles in contact, $R_{\text{binary}} = \sqrt{5/3}\, s_0$ (see Chapter 4). Aggregates larger than the transi-

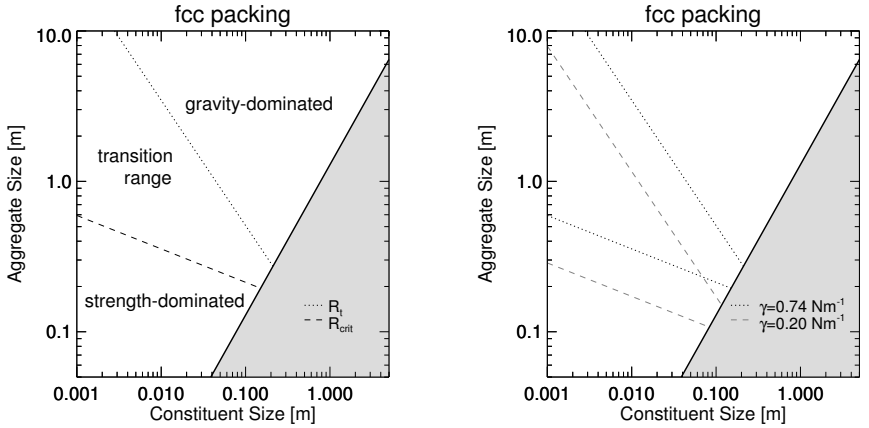

(a) transition range

(b) different adhesion strength

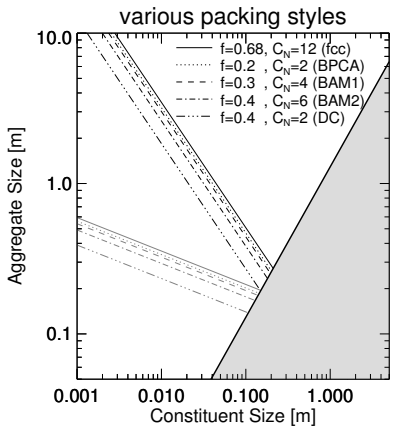

(c) different packings

Figure 3.4: Strength- and gravity-dominated regimes: Variability with surface free energy is comparable to variability across different aggregate packing styles. Different fragmentation outcomes described by the power-law distributions above yield $Q^\star_{\text{min}}$ within the transition regime. Critical R_{crit} (dashed line) and transition radius R_{t} (dotted line) mark its boundaries. The gray-shaded are mattes non-existing aggregates.

tion radius lie within the gravity-dominated regime and those smaller than the critical size within the strength-dominated regime (see Fig. 3.4(a)). The transition regime constitutes part of the strength regime, where different fragment size distributions yield slightly different $Q^\star$, whereas aggregates at the critical radius are most vulnerable to

destruction as this yield only two fragment halves (cf. Fig. 3.2). Figure 3.4(b) shows the dependence on the surface free energy γ within our chosen minimum and maximum value. Different packing styles, expressed by their internal filling factor and corresponding coordination numbers, are illustrated in Fig. 3.4(c). The resulting variability in both $R_{\rm crit}$ and $R_{\rm t}$ is comparable to their variability with γ. In Chapter 4, Sec. 4.2 we will directly identify amorphous packing styles of more realistic aggregates with the average bulk properties used here (cf. Figs. 4.5 and 4.6). Interestingly, in this way we obtain a qualitatively similar division into strength and gravity regime as reported by e.g., Love and Ahrens (1996) and Benz and Asphaug (1999).

Chapter 4

Aggregate Models - numerical

The theory presented in Chapter 3 deals with the resistivity of aggregates. In this chapter the analytical expressions derived for regularly packed aggregates in Secs. 3.1 and 3.2 will be compared to a more realistic random arrangement of particles. In order to carry out this comparison aggregates of various packing styles are created numerically. As before, all aggregates are made of one material type. Regularly and randomly packed aggregates are considered: Firstly, aggregates built of equal-sized monomers arranged in close regular packings including face-centered cubic (fcc) and body-centered cubic (bcc) structure; secondly, amorphous configurations like ballistic particle cluster aggregates (BPCA). We investigate classic BPCAs and various modifications to their configuration, including the standard modifications BAM1 and BAM2 (ballistic aggregates with one or two migrations, see below for details – Shen et al., 2008). Different constituent size distributions and aggregate density constraints are also considered. Using various numerical approaches their specific self-energy Q and specific break-up energy $Q^\star$ will be numerically computed. Finally, these will be compared to the analytical results in the previous Chapter.

In order to better describe the size of both crystal-like and fractal-like agglomerates, which may feature both irregular surfaces and irregular shapes, we employ the characteristic radius R_c, related to the gyration radius R_g, which is commonly used in polymer and proto-planetary science (e.g. Mukai et al., 1992; Lobanov et al., 2008). Let $\vec{r}_i$, s_i, and m_i be the location, size, and mass of the i-th constituent, then $M = \sum_i^N m_i$ and $\vec{r}_c = \sum_i^N (m_i \vec{r}_i)/M$ denotes the total mass and center of mass of the aggregate. Then,

$$R_g = \sqrt{\frac{\sum_i m_i (\vec{r}_i - \vec{r}_c)^2}{M}} \text{ and} \tag{4.1}$$

$$R_c = \sqrt{\frac{5}{3}} R_g \,. \tag{4.2}$$

Here the characteristic radius R_c denotes the radius of a homogeneous sphere with a gyration radius equivalent to that of the aggregate. In general, R_c describes the actual size of an agglomerate including close-packings, classic BPCAs, and those with internal size distributions as well. In Fig. 4.1 we illustrate the characteristic and gyration radii by a classic BPCA with 5000 particles.

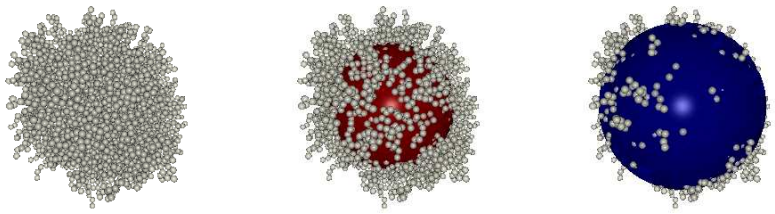

(a) (b) (c)

Figure 4.1: We use the characteristic radius R_c to describe the aggregate radius consistently referred to as R. It is based on the gyration radius R_g– see equations (4.1) and (4.2). These are illustrated by a BPCA made of 5000 mono-sized particles: (a) the actual aggregate, (b) aggregate and corresponding sphere of gyration radius R_g, and (c) aggregate and corresponding sphere of characteristic radius R_c.

4.1 Regular Packings

We arrange individual particles into larger agglomerates using the characteristic bulk properties of regular packings (listed in Table 3.1) and the corresponding lattice structures. Figure 4.2 shows examples of fcc and bcc aggregates. These organized, crystal-

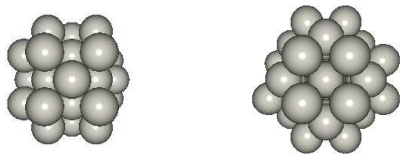

(a) (b)

Figure 4.2: Aggregates composed of close-packed equal spheres: (a) face-centered cubic (fcc) and (b) body-centered cubic (bcc) configuration. These regular, crystal-like arrangements yield high coordination numbers and thus high filling factors (cf. also Table 3.1)

like packings of single-sized constituents achieve relatively high coordination numbers which results in both high filling factors (high internal density) and high connectivity. This implies an extended strength regime and generally larger self-energies Q. As discussed in Chapter 3, Sec. 3.1 high coordination number directly affect aggregate properties like resistivity. The analytical mean field calculations (Eq. (3.3)) used the bulk coordination number given in Table 3.1, the effects of the free aggregate surfaces – surface energy and surface tension – were neglected. The consequence of this simplification as a function of aggregate size radius (R) is demonstrated in Fig. 4.3 by comparing numerical and analytical calculations of the adhesive self-energy for various aggregate sizes. The exact numerical computation of the self-energy, taking into account surface effects, is achieved by implementing the most general Eq. (3.3) and then dividing by the aggregate mass M. In Fig. 4.3 we have plotted the adhesive contribution to the self-energy Q. The relative error of using the mean-field equation is about 15% for 1 m aggregates with $s_0 = 10\,\mathrm{cm}$ and it vanishes for larger aggregates.

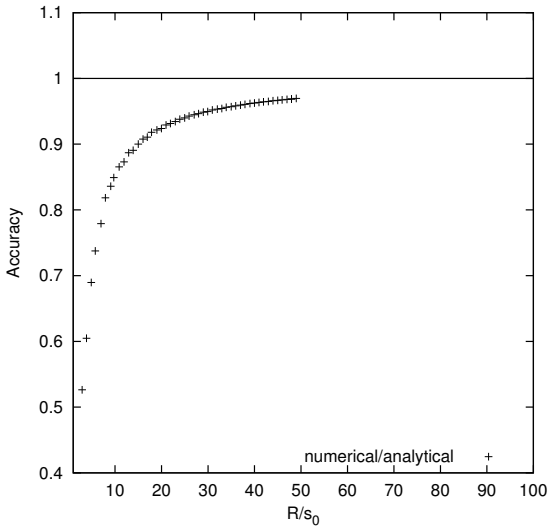

Figure 4.3: Comparison of the analytical and numerical specific adhesive self-energy (2nd term in Eq. (3.18)) for fcc agglomerates made of 10 cm-sized constituents. The discrepancy due to neglected surface effects vanishes with $R \to \infty$.

To address the question of how much energy is required to split an aggregate we will follow two different approaches: 1) a semi-analytical and 2) a purely numerical approach. We will then compare these two results with those obtained from Eq. (3.18). For simplicity, we will concentrate on splitting an aggregate into halves and therefore consider only a single fracture plane.

1. The semi-analytical approach: We first numerically calculate the adhesion self-energy E_{A} as defined in the second term of Eq. (3.3). Then we apply the analytical approach outlined in Eq. (3.10) in Chapter 3, Sec. 3.2, where we introduced an adhesion energy density $\bar{\gamma}$. Using $\bar{\gamma}$, we then calculate the specific break-up energy for the surface area $S = \pi R^2$ and crack width s_0.

2. The purely numerical procedure: Mimicking a cracked surface we define a plane which intersects the center of mass of the aggregate. We then identify which bonds intersect that plane and declare these to be broken. Finally, we count the number of bonds broken.

Figure 4.4 shows a comparison between the analytical, semi-analytical, and purely numerical approach to obtain an aggregate specific break-up energy. Both semi-analytical and numerical approaches are within $10-15\%$ of the analytical estimates for aggregates where $R/\langle s\rangle \approx 10$. If $R/\langle s\rangle < 10$ accuracy drops to within 70% as the aggregates comprises merely ~ 500 or fewer individual particles. Naturally, the accuracy improves as $R \to \infty$ and thus $N \to \infty$. The constituent size typically used in the following sections is about 1 cm while aggregates are grown to at least decimeter size and beyond. For these aggregates we estimate our inaccuracy to be at most 15%.

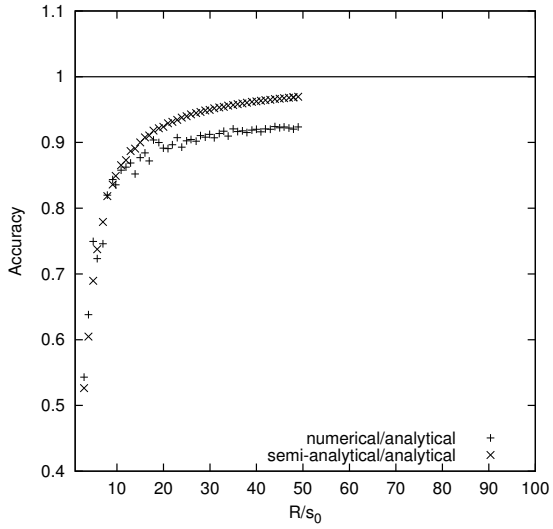

Figure 4.4: Comparison of the analytically, semi-analytically, and numerically obtained specific break-up energy (adhesive part only) needed to split an aggregate into two *halves*. Results are shown for fcc aggregates with constituents of 10 cm. Both semi-analytical and numerical approaches are within $10-15\%$ of the analytical estimates.

4.2 Random Packings

Random arrangements of equal hard spheres have been used to model a variety of physical problems (Mrafko and Duhaj, 1974). In planetary science, these Ballistic Particle

Cluster Aggregates (BPCA) have widely been used for the study of asteroids and planetary formation (Richardson, 1995; Dominik and Tielens, 1997; Mukai et al., 1992; Kolokolova et al., 2007; Shen et al., 2008, 2009), employing the standard method to create randomly arranged aggregates (e.g. Vold, 1959; Mukai et al., 1992). In our implementation of the classical BPCA method we proceed as follows: A seed particle is placed at the origin of a spherical coordinate system. Further constituents are added in a "hit and stick" mechanism (Dominik and Tielens, 1997) after following random ballistic trajectories. These trajectories are determined by drawing from uniformly distributed spherical angles while randomly choosing a target particle among the current aggregate constituents. Using this method we obtain rather fluffy aggregates. In order to achieve higher coordination numbers and thus higher filling factors, we have also introduced three different modifications to the simple BPCA algorithm:

1. BAM1 – ballistic agglomeration with one migration – requires that each newly added constituent has at least two contacts. That is, after the constituent reaches one particle, it "migrates" to the nearest second constituent, by rolling or sliding over the first.

2. BAM2 – ballistic agglomeration with two migrations – requires that each newly added constituent has three contacts. This is achieved by performing two BAM1 migrations in sequence along the shortest possible trajectory.

3. DC – density-constrained – requires that a newly added constituent can only be "accepted" if the whole aggregate matches a minimum density. In particular, every time a new constituent is added we calculate the radius of a homogeneous sphere of given density using the current aggregate mass. If the distance between the contact point of the new constituent and the center of mass of the aggregate is smaller than this radius, the constituent is accepted, otherwise it is rejected

and a new particle is chosen randomly. Here we choose a pre-defined aggregate density $\rho_{\rm agg} = 400\,{\rm kg\,m^{-3}}$ in order to match ring particle densities inferred from Cassini observations (e.g. Tiscareno et al., 2007; Porco et al., 2007; Robbins et al., 2009; Colwell et al., 2009). Note that this procedure, unlike BAM1 and BAM2, is not strictly in the line of the BPCA philosophy as it modifies the pure random placement with a conditional random placement of particles. One could consider that this method mimics reorganization of constituents due to mutual collision and thus describing compaction.

In addition to the geometric modifications listed above (for BAM1 and BAM2 see also Shen et al., 2008) variable consituent size distribution $n(s)$ is also allowed. We primarily consider power-law distributions given by

$$n(s) \;=\; N\frac{(1-k)}{(s_{\rm max}-s_{\rm min})}s^{-k}. \tag{4.3}$$

In the case of monomers of size s_0 this distribution simply reads $n(s) = N\delta(s-s_0)$. Figure 4.5 shows examples of all the different randomly packed aggregates used in this work. These include mono-sized classic BPCA (a), density-controlled (b), BAM1 (c) and BAM2 (d). Further BPCAs with size distributions with $k = 0$ (uniform) (f), $k = 3$ (g), and $k = 5$ (h) using $s \in [0.001, 0.1]\,{\rm m}$ and $s \in [0.01, 0.1]\,{\rm m}$ have been applied. In the case of mono-sized aggregate we choose cm-sized constituents ($s = 0.01\,{\rm m}$). These size ranges are motivated by particle size distributions of Saturn's rings inferred from Voyager and Cassini observations (Marouf et al., 1983; French and Nicholson, 2000; Zebker et al., 1985). Figure 4.5 shows one example of each of the packing styles considered in this study.

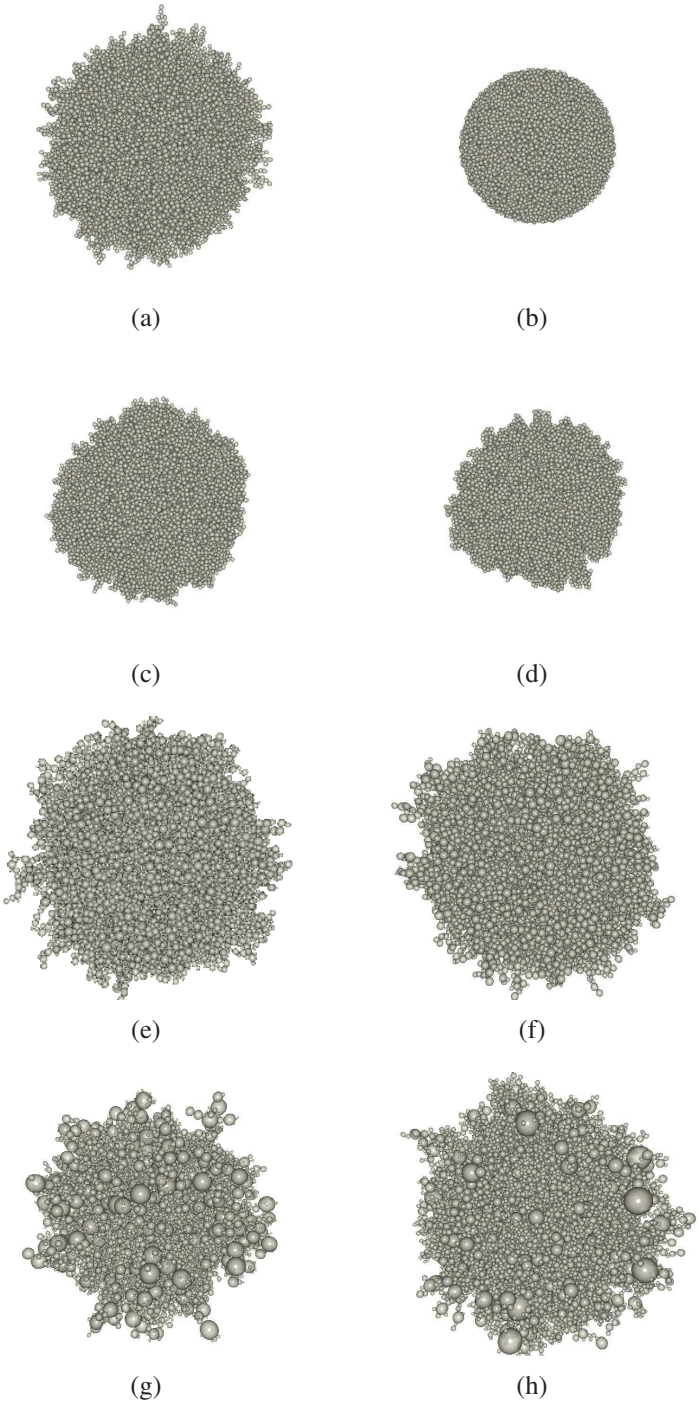

Figure 4.5: BPCA and modified BPCAs with 25000 constituents each. *Top two rows:* mono-sized agglomerates where (a) classic BPCA, (b) CD at $400\,\mathrm{kg\,m^{-3}}$, (c) BAM1, and (d) BAM2. *Bottom two rows:* Clusters made of particles with size distribution: (e) $k = 0$ (uniformly distributed) between $s \in [0.1 - 10]\,\mathrm{cm}$, (f) $k = 0$ between $s \in [1 - 10]\,\mathrm{cm}$, (g) $k = 3$ between $s \in [0.1 - 10]\,\mathrm{cm}$, and (h) $k = 5$ between $s \in [0.1 - 10]\,\mathrm{cm}$.

Bearing in mind that relative impact velocities in unperturbed planetary rings are in the order of $\mathrm{mm\,s^{-1}}$, collisions occur at sufficiently low speed to enable aggregation by adhesion (e.g. Hatzes et al., 1991). Therefore, this "hit and stick"- mechanism of aggregation (Dominik and Tielens, 1997), where all colliding particles have a probability of sticking close to unity, provides an adequate method. However, these collisions do not involve, or only involve a few internal re-structuring of the aggregates. The resulting aggregates are fluffy in nature and typically show very low internal densities.

Figure 4.6 shows the internal filling factor f of different aggregates as a function of distance from the center of mass of aggregate. We mark the characteristic radius for each of the aggregate examples (vertical lines). Typically, f slowly decreases with distance from the center, approaching a global average value. These average aggregate properties are found beyond the characteristic radius, where the filling factor rapidly drops. "Fingery" structures form the outermost shell of the aggregate (compare also Fig. 4.1) and are a typical outcome of the "hit and stick" formation process (Dominik and Tielens, 1997). In the case of classic BPCAs the filling factor is low, $f \approx 0.2$. Even if the aggregate has an internal size distribution (Figs. 4.6(c) and 4.6(d)) the filling factor is comparable to the classic BPCA (Fig. 4.6(a)). Although one might expect a denser packing when lowering the smallest size of the size distribution s_{min}, the random direction of particle placement prevents smaller particles from filling the gaps. Only modifying the aggregate formation process alters the aggregate properties, e.g. Fig. 4.6(b) shows BAM1 and BAM2 require multiple particle contacts resulting in a tighter packing and thus higher filling factors. Similarly, in the case of controlled internal density (DC) the filling factor is actively determined and therefore matches the fixed aggregate density with $f \approx 0.4$. Directly related to the filling factor are the average coordination numbers. BPCAs with and without size distribution have coordination numbers of approximately 2, since their formation processes are the same.

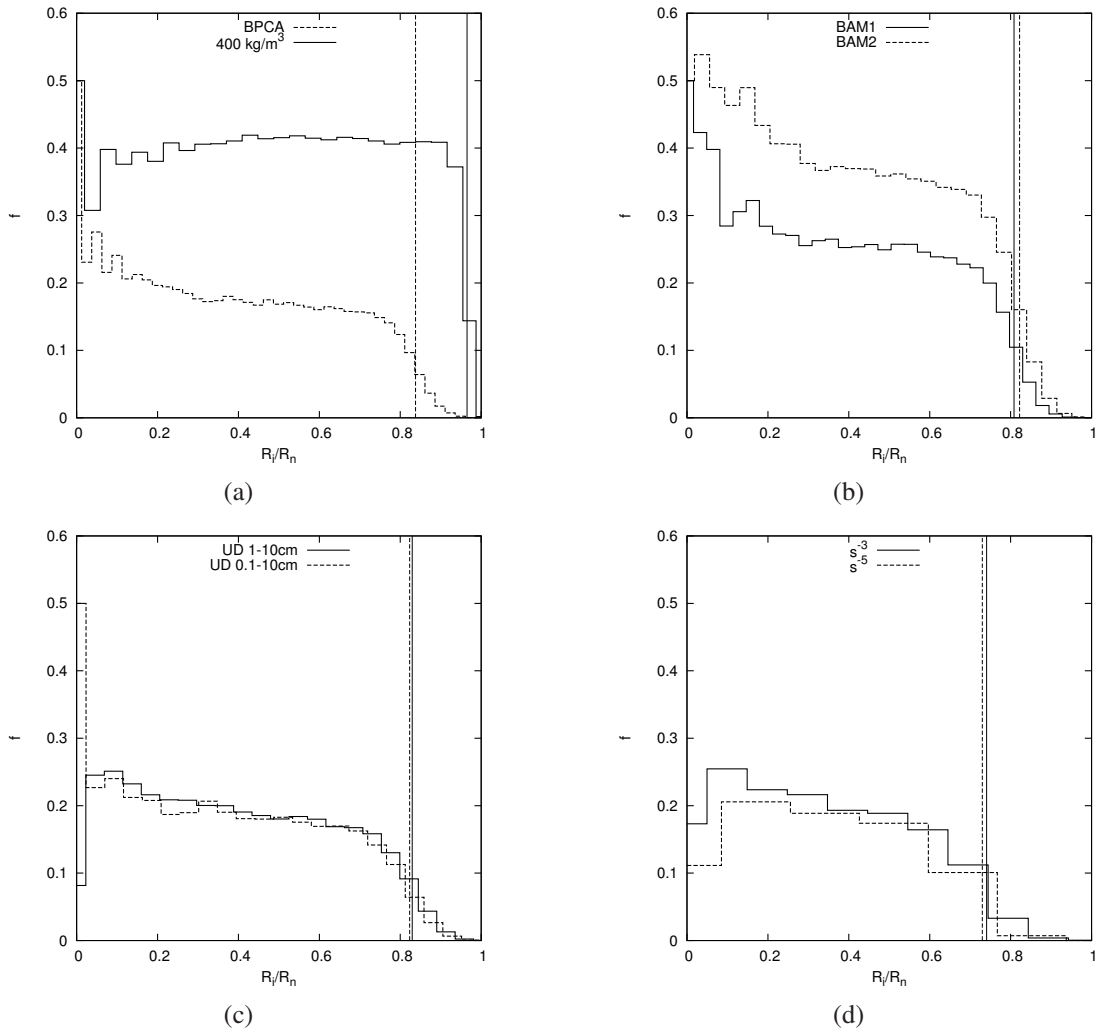

Figure 4.6: Filling factor distributions as a function of normalized distance from the center of the aggregate R_i/R_n, where R_n is the radial distance of the outermost constituent: (a) BPCA and DC, (b) BAM1 and BAM2, (c) BPCA with uniform size distributions ($s \in [1-10]$ cm and $s \in [0.1-10]$ cm), and (d) BPCA with size distributions of slope $k = 3$ and $k = 5$ between $s \in [0.1-10]$ cm. Vertical lines mark the position of the characteristic radius R_c. Here, each aggregate consists of 30000 particles.

Coordination numbers are only higher if the geometric packing conditions, and thus the arrangement of constituents, is changed. This is independent from the constituent size distribution. Thus, BAM1 and BAM2 modified aggregates have by definition $C_{\mathrm{N}} \approx 4$ and $C_{\mathrm{N}} \approx 6$, respectively. This is also true for the density-controlled aggregates, where the only difference in forming them is that more mass is packed into the same volume.

In the case of aggregates made of equal-sized particles a higher coordination number directly implies a higher adhesive self-energy, but this correlation between coordination number and adhesive self-energy is not necessarily true for aggregates with size distributions, since bond strength also depends on the effective size of the particles in contact. Also, we did not find a suitable average constituent size for a given distribution that would satisfy this proportionality.

We have created aggregates of various sizes for each packing style. Unless using a designated size distribution we evaluated the aggregates for $s_0 = 1\,\mathrm{cm}$. Specific self-energies were calculated for each of these according to Eq. (3.3). The specific break-up energies were inferred using the semi-analytical approach for all BPCAs with equal-sized constituents and the purely numerical approach for those having an internal size distribution. Figures 4.7 and 4.8 show the specific energies for all aggregates. Each cross marks one aggregate. Lines are fitted to the data points.

Despite the generally lower specific adhesion energies, the transition size associated with the classic BPCA aggregates in Fig. 4.7(a) of $R_\mathrm{t} \approx 3.1\,\mathrm{m}$ is comparable to that of regular packed aggregates (cf. Fig. 3.3) as their relatively low filling factor f reduces their self-gravity. This, however, implies significantly smaller break-up energies (on the order of one magnitude), consistent with what is generally expected for loosely-packed aggregates. This results in critical sizes around 0.3 m. The aggregates types BAM1 and BAM2 show slightly larger transition and critical sizes given both their higher coordination number and filling factors (see Figs. 4.7(c) and 4.7(d)). A similar result is obtained for the DC aggregates in Fig. 4.7(b). Despite having a slightly denser packing the DC aggregates have a smaller transition size at $R_\mathrm{t} \approx 1.8\,\mathrm{m}$; this is because DC has a coordination number of $C_\mathrm{N} \approx 2$, similar to classic BPCAs. The inclusion of a constituent size distribution generally reduces the specific adhesion energy and

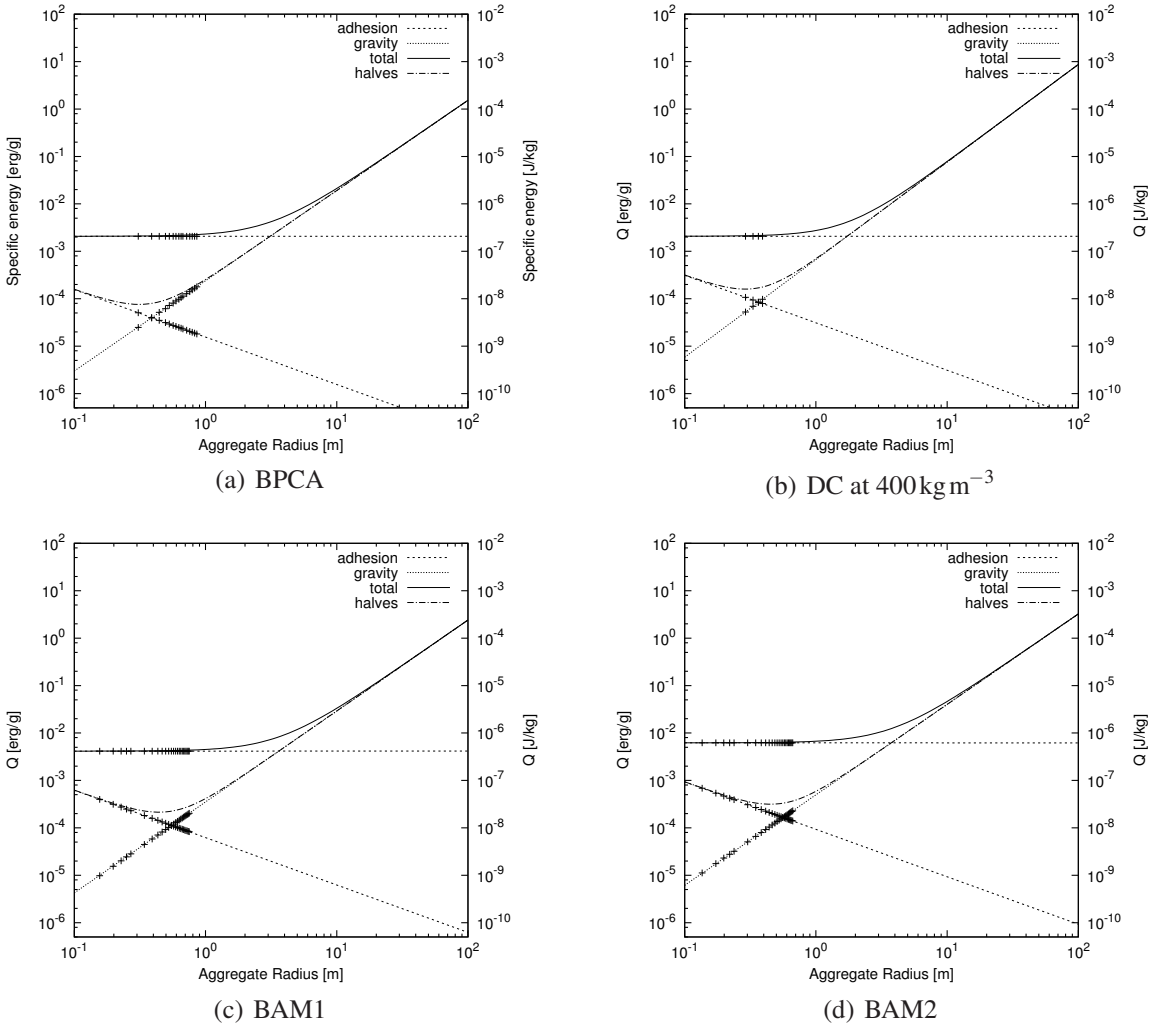

(a) BPCA

(b) DC at $400\,\mathrm{kg\,m^{-3}}$

(c) BAM1

(d) BAM2

Figure 4.7: The specific energy (self-energy/mass) vs. radius of different BPCAs with equal-sized constituents. Each cross denotes one aggregate where we split the adhesive and gravitational contributions. Lines are fitted to the data points. All aggregates are made of 1 cm-sized constituents.

consequetly, the critical sizes when compared to the classic BPCA (see Fig. 4.8). As a consequence, these aggregates are more easily disrupted. In general, aggregates with internal size distributions have significantly smaller transition sizes. We note that the DC aggregate has nearly the same R_t as the aggregate with a $k = 5$ distribution. In general, however, critical sizes lie within a few decimeters regardless of packing style. Table 4.1 summarizes these findings.

Packing	Specification	s[cm]	C_N	f	R_{crit}[m]	R_t[m]
BPCA		1	2	0.2	0.30	3.11
BAM1		1	4	0.3	0.36	3.62
BAM2		1	6	0.4	0.37	3.37
DC	$\rho_{agg} = 400\,\mathrm{kg\,m^{-3}}$	1	2	0.4	0.21	1.73
SD	$k = 0$	1-10	2	0.2	0.18	0.50
SD	$k = 0$	0.1-10	2	0.2	0.18	0.50
SD	$k = 3$	1-10	2	0.2	0.22	1.00
SD	$k = 5$	1-10	2	0.2	0.29	1.85

Table 4.1: Properties of various randomly packed aggregates including constituent size range s, coordination number C_N, filling factor f, and critical R_{crit} and transition radius R_t.

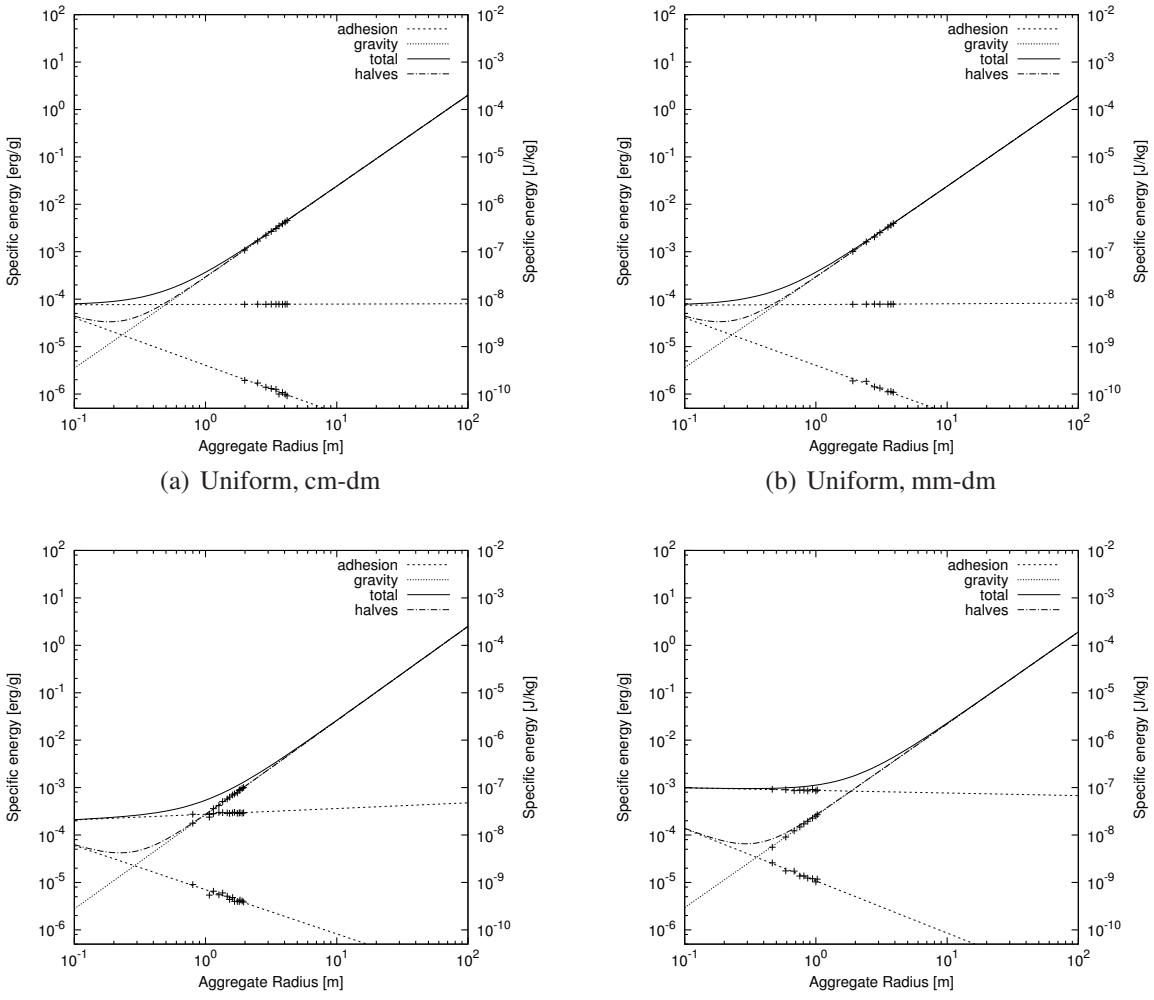

(a) Uniform, cm-dm

(b) Uniform, mm-dm

(c) $k = 3$, mm-dm

(d) $k = 5$, mm-dm

Figure 4.8: The specific energy (self-energy/mass) vs. radius of different BPCAs with internal size distribution. Each cross denotes one aggregate where we split the adhesive and gravitational contributions. Lines are fitted to the data points.

Chapter 5

Ring application – collisional velocities

The specific self-energy of aggregates for a wide range of packings have been calculated in the preceding Chapters 3 and 4. The self-energy proved to be the determining factor in calculating the transition size separating the strength and gravitational regimes. Furthermore, it denotes the limit for a complete disruption of an aggregate. Most of the differences between particular aggregate types are due to differences in their internal mass density and average coordination number. Further, we have estimated the specific break-up energy and find a good qualitative agreement with laboratory experiments and impact simulations (Love and Ahrens, 1996). We saw that, in particular, the BPCA and their modifications are aggregates that may resemble the under-dense fragile structure formations in the rings, representing the reality of them.

Now we shall apply the results from the previous chapters to Saturn's ring. For this application it is necessary to emphasize the following: the ring particles seem to be compacted aggregates with a filling factor of around 0.4 (ice material). It is also likely that aggregates which are more compact have coordination numbers (C_N) higher than in the BPCA model, but the C_N should not be as high as in a crystal-like packing.

Therefore, these assumptions bring us to conclude that the BAM2 model is a good match for ring aggregates, which has the $C_N = 6$ and the $f = 0.4$.

We want to define the critical velocity for collisions needed for fragmentation of both aggregates. Fragmentation can occur when the kinetic energy of the two impacting aggregates of radius R_1 and R_2 is large enough to split both collision partners into two pieces

$$E_{\text{kin}} > W(R_1) + W(R_2)\,. \tag{5.1}$$

The Eq. (5.1) is limited for cases of very low collisions velocities (mm/s). Re-ordering of the constituents forming the aggregate is not considered and adjustments related to energy dissipation may be addressed by a constant. Despite we neglect some physics involved (that would indeed mean molecular dynamics simulations), we will show that the results match the expectation and information we have for particles in the rings.

In Chapter 3, Sec.3.2 we defined the work required to split an aggregate as

$$W(R) \;=\; -Q^{\star}(R)\cdot M(R) \tag{5.2}$$

where $Q^{\star}$ is specific break-up energy defined by Eq. (3.18) which can be rewritten as

$$Q^{\star}(R) \;=\; -\alpha_{\text{A}} R^{-1} - \alpha_{\text{G}} R^{2}\,, \tag{5.3}$$

where α_{A} and α_{G} are defined in Eqs. (3.19). The kinetic energy of the impact is given by

$$E_{\text{kin}}(M_1, M_2) = \frac{M_{\text{eff}}}{2} g^2\,, \tag{5.4}$$

where the effective mass is defined by $M_{\rm eff} = M_1 M_2/(M_1+M_2)$ and g is the relative velocity of the collision partners.

Rewriting Eq. (5.1) considering $R_1 \propto M_1^{1/3}$ and $R_2 \propto M_2^{1/3}$ we have

$$g(R_1,R_2)^2 > g_{\rm frac}(R_1,R_2)^2 = 2\,(R_1^3+R_2^3)\,\frac{[\alpha_{\rm A}(R_1^2+R_2^2)+\alpha_{\rm G}(R_1^5+R_2^5)]}{(R_1^3\cdot R_2^3)}, \qquad (5.5)$$

which gives the critical velocity $g_{\rm frac}(R_1,R_2)$ when fragmentation is the dominating in the outcome of collision.

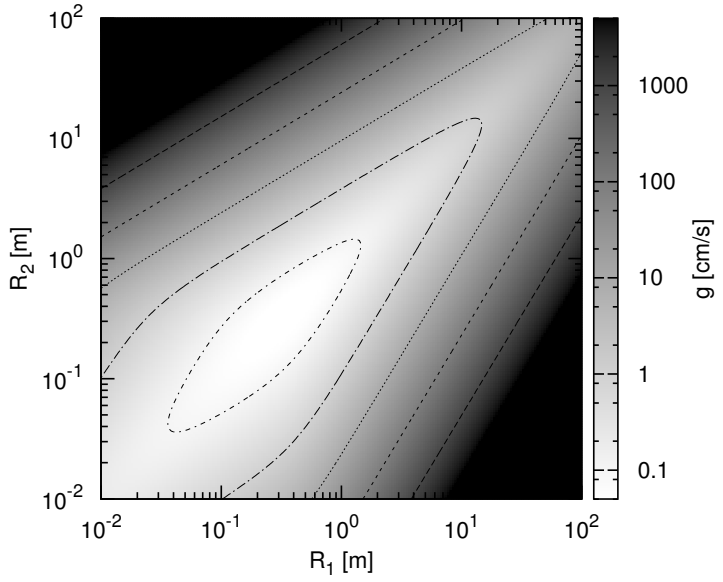

Figure 5.1: Contour plot for different critical fragmentation velocities $g_{\rm frag}(R_1,R_2)$, see Eq. (5.5). Constituents with radii s = 1 cm, $\gamma = 0.74\,{\rm N\,m^{-1}}$ and $C_N = 6$ have been used.

Figure5.1 shows the contours for different critical fragmentation velocities $g_{\rm frac}(R_1,R_2)$. As one can see, for a given velocity complete fragmentation is only possible for distinct

region of sizes considering $R_1 = R_2 = R$

$$R_{\min} = \frac{8\alpha_A}{g^2} < R < \frac{g^2}{\sqrt{8\alpha_G}} = R_{\max}\,. \tag{5.6}$$

Additionally, one should note, that only agglomerates of similar size can effectively destroy each other, if this condition is not met the larger body usually survives. Using $\gamma = 0.2\,\mathrm{N\,m^{-1}}$ instead of $\gamma = 0.74\,\mathrm{N\,m^{-1}}$ would decrease α_A and thus $R_{\min}$ by a factor of about 10. Likewise, the maximum impact velocity for aggregation to occur g_{agg} may be found in a similar way. Aside from minimum and maximum sizes in the rings one may obtain the ring particle size distribution by using these results on threshold velocities in kinetic calculations (see Chapter 6).

5.1 F ring Analysis

We will now draw some conclusions for Saturn's F ring, based on our preliminary considerations. As mentioned in the introduction, this thin, kinky ring is shepherded and perturbed by the moons Prometheus and Pandora. The perturbations of the moons induce large relative velocities of the particles of the order $\mathrm{m\,s^{-1}}$ (e.g. Beurle et al., 2010). In less perturbed regions one should expect $\mathrm{dm\,s^{-1}}$. The ring has a large amount of dust particles ($1 - 100\,\mu$m).

Fig. 5.2 shows the specific splitting energies $Q^\star$. Additionally, the corresponding specific kinetic energies are plotted for different collision velocities, where the crossing points with the $Q^\star$ lines correspond to the minimal and maximal R as given by Eq. (5.6). Thus, the dust particles can adhere to agglomerates with radii of around 1 cm in the less perturbed regions ($1\,\mathrm{dm\,s^{-1}}$), but will be destroyed in the perturbed

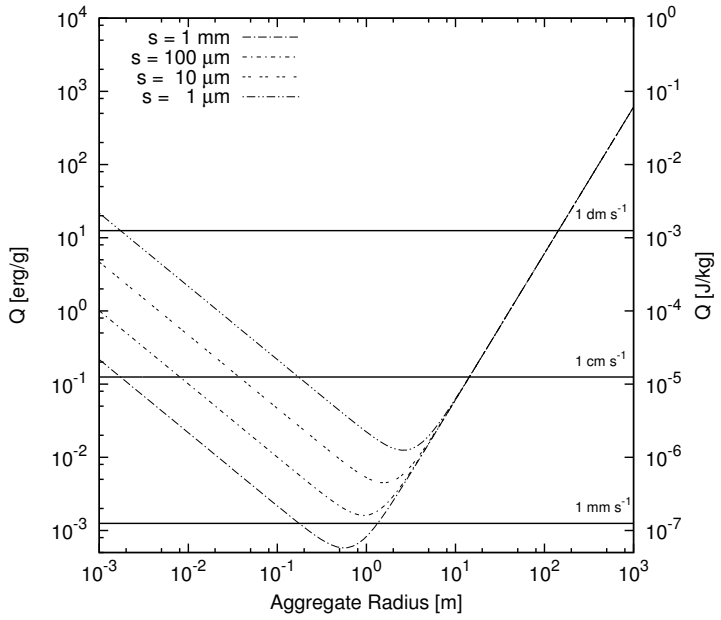

Figure 5.2: The plot shows the specific splitting energies for the BAM2 aggregates with different constituent sizes ($\gamma = 0.74$ N m^{-1} and $C_N = 6$). Additionally, the kinetic energies are plotted for different collision velocities. The crossing points correspond to limits of the fragmentation zone, where fragmentation of both collision partners can be observed.

regions (1 m s^{-1}). Further growing will be limited because of ongoing fragmentation, and thus, decimeter and meter aggregates should be rare in the F ring. Thus, km sized aggregates can only be formed due to compression of ring material in the regions perturbed by the moons Prometheus and Pandora. If some of the aggregates do grow above the maximum limit ($R_{\max} > 100\,\mathrm{m} - 1\,\mathrm{km}$), they can grow even further, but these are transient bodies and they are likely disrupted by a gravity encounter with Prometheus. Thus, in the F ring we expect to observe a three-modal size distribution as observed (Showalter et al., 1992; Beurle et al., 2010) with micrometer-sized dust, medium sized centimeter agglomerates (parent bodies for dust; Bodrova et al., 2012) and a few km or larger sized agglomerates.

5.2 Dense Rings Analysis

For the inner dense rings the environment differs greatly from that of the F ring. In this environment tidal forces and impacts between the aggregates lead to their disruption and formation of transient structures called self-gravity wakes. Particles inside a single self-gravity wake have very low relative velocities whereas the relative velocity between neighboring self-gravity wakes could be of the order of the Toomre wavelength times the orbit frequency (Daisaka and Ida, 1999), this is a favorable environment for the formation of adhesive bounds. In the following we want to estimate a critical thermal velocity to treat gravo-adhesive aggregates (sizes R_1 and R_2) in mutual collisions. The collisional velocity between two aggregates depends on two factors: *(i)* the thermal velocity $v_{\rm th}$ of the ring particles and *(ii)* on the relative velocity caused by the shear motion $(2/3)\,\Omega(R_1+R_2)$. Thus, we estimate the collisional velocity by

$$g \approx v_{\rm th} + \frac{2}{3}\Omega(R_1+R_2)\,. \tag{5.7}$$

Instead of the shear velocity one can also consider the escape velocity, which is of the same oder of magnitude and has the same dependence R. The thermal velocity dominates the impacts of small aggregates, whereas the shear is more important for collisions between larger bodies. Simulations including only restitutive collisions and different particle sizes have shown a rather weak dependence of the thermal velocity, $v_{\rm th}$, on the radius of the particles, therefore, we will consider a size independent thermal velocity at the moment, for simplicity. However, because the larger particles dominate the thermal motion of the particle ensemble due to their larger masses, we can relate it to the size of the large particle

$$v_{th} \approx \frac{4}{3}\Omega R_2 \tag{5.8}$$

with $R_1 << R_2$. Substituting Eq. (5.7) into Eq. (5.5) we can calculate the critical thermal velocity needed to split both collision partners again adhesive and gravitational resistivity (α_A and α_G)

$$v_{\rm th}(R_1,R_2) > \sqrt{2\,(R_1^3+R_2^3)\,\frac{[\alpha_{\rm A}(R_1^2+R_2^2)+\alpha_{\rm G}(R_1^5+R_2^5)]}{(R_1^3\cdot R_2^3)}} - \frac{2}{3}\Omega(R_1+R_2)\,. \quad (5.9)$$

In Fig. 5.3 the critical thermal velocity has been plotted for different radii R_1 and R_2. Similar to Fig. 5.1 the Fig. 5.3 shows the contours for different critical thermal veloc-

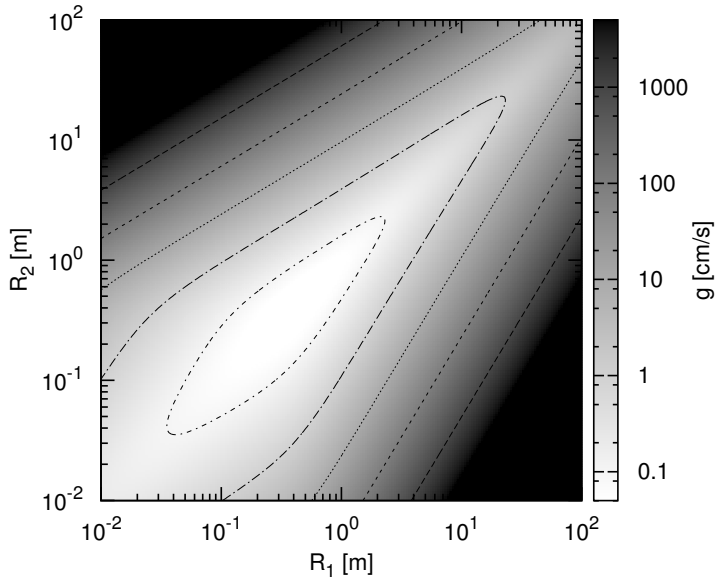

Figure 5.3: The contour plot shows the critical thermal velocities for fragmentation, see Eq. (5.9). Constituents with radii s = 1 cm, $\gamma = 0.74\,\mathrm{N\,m^{-1}}$ and $C_N = 6$ have been used.

ities, and again, as one can see, for a given velocity complete fragmentation is only possible for distinct regions of sizes following Eq. (5.6). Small particles ($< R_{min}$) will accrete steadily to larger particles. If the aggregate radius is larger than the minimal radius R_{min} it will likely be destroyed by particle of same size or larger. Thus, these

particles undergo a steady growing and destruction limiting their numbers. Therefore they are less numerous than the particles with size R_{min}. In reality the number density falls off with a power law $n \propto R^{-3}$. The larger particles are under the gravitational regime where the growth is limited by tidal forces. In this case of self-gravity wakes R_{max} will rather correspond to the wavelength $\lambda_{wake} \approx 20 - 50$m.

There is little known about the agglomerate "constituents" sizes in Saturn's rings. It should be between the observed minimal observed ring particle radius of around 1 cm (French and Nicholson, 2000) and the typical regolith grain radius of around 10 μm observed on top of the ring particles (Nicholson et al., 2008). The observed minimal ring particle aggregate radius is between 1 cm and 30 cm, which implies constituent radii larger than 0.1 mm and smaller than 1 cm for the considered velocity range of 1 mm s^{-1} and 3 mm s^{-1} using our estimates from above. These constituent sizes will deliver reasonable $R_{\min}$ in the expected velocity range. However, one should note, if the thermal velocity of the ring particles exceeds 3 mm s^{-1} constituents of tens of micrometer deliver good result for $R_{\min} \approx 50$ cm. The calculated maximal agglomerate radii calculated from the assumed thermal velocities are between 8 and 23 meters (for velocities between 1 and 3 mm s^{-1}). These estimates reproduce the correct order of magnitude for the size range, they are of preliminary character but demonstrate the relevance of the results gained in this work. As a next step one should apply these results to kinetic calculations to obtain a size distribution for the particles in the ring. To achieve this, one must first estimate the maximum impact velocity, $g_{\rm agg}$, where aggregation can occur (Spahn et al., 2004; Albers and Spahn, 2006; Albers, 2006). This relation can be found in the same way as $g_{\rm frac}$. Nevertheless this aim, as well as the self-consistent treatment of self-gravity wakes, are out of the scope of this Thesis.

Chapter 6

Discussions and conclusions

In this work we have studied the role of contact forces (adhesion) for the aggregation and fragmentation of aggregates in a granular gas (planetary rings) by calculating their specific (per mass) binding energies $Q^\star$ in relation to their gravitational self-energy. We have investigated several types of aggregates, including regular packed (fcc, bcc) and randomly build ballistic aggregates (BPCA), also including a constrained density (DC) as well as reordering of the constituents (BAM1, BAM2). One should note that the BPCA and fcc aggregates, which have filling factors between 0.2 and 0.74 and coordination numbers between 2 and 12, represent two limit cases for a realistic aggregate. We can say that the frequent collisions in planetary rings, which pack, reorganize, and disintegrate particles, lead to neither organized nor very densely packed aggregates. Therefore, amorphous packing can better represent the aggregates formed in the ring environment as concluded from Cassini observations.

We have been able to estimate the resistivity of granular aggregates between strength- and gravity regimes as observed in material sciences or in asteroidal studies. We have shown that early in their formation, in the strength regime, the contact forces are those

ones that support the aggregates the most, i.e. adhesion is the major player for their resistivity corresponding to the strength regime. In contrast larger boulders are dominantly held together by their mutual gravity (gravitational regime). Consequently, the energy necessary to disrupt or erode an aggregate is a function of the aggregate size, in terms of energy per mass (specific energy) we have $Q^\star(R)$. In the strength regime $Q^\star(R)$ is inversely proportional to the aggregate size ($Q^\star(R) \propto R^\zeta$) and reaches its minimum before the gravitational specific binding energy dominates ($Q(R) \propto R^2$, cf. Fig. 3.2). The exponent ζ depends on the damage ratio of the target aggregate, it assumes values between -1 and 0, and it is related to the size distribution of fragments (and to the exponent p in Chapter 3, Sec. 3.2): $\zeta = -1$ corresponds to splitting the aggregate into two equally sized fragments, whereas $\zeta = 0$ implies total fragmentation into all individual constituents as the specific fragmentation energy transforms into the specific adhesive binding energy $Q^\star(R) \to Q$ which is independent of the aggregate size R. From this work we conclude that the transition between the strength and the gravitational regimes is located along Q line, all others measurement for $Q^\star$ are intermediate stages of rupture.

Mutual collisions between the aggregates are capable to change the sizes of the composite ring particles (however, aggregates can also be destroyed tidally). This may occur either through aggregation for impacts at low velocities, or alternatively, due to fragmentation at higher collision velocities. The collision dynamics and the resistivity of the aggregates determine these velocity thresholds g_{agg} and g_{frag}, where g_{frag} was estimated in Chapter 5. We have shown that knowledge of the critical fragmentation velocity provides us with information about the agglomerate size distribution through the minimal and maximal aggregate radius. The difference of both velocities, $g_{\mathrm{agg}} - g_{\mathrm{frag}}$, is determined mainly by the dissipation that occurs during collisions between the constituents of both aggregates. This dissipation arises from the viscous deformations and

from the irreversibility of formation and destruction of single contacts.

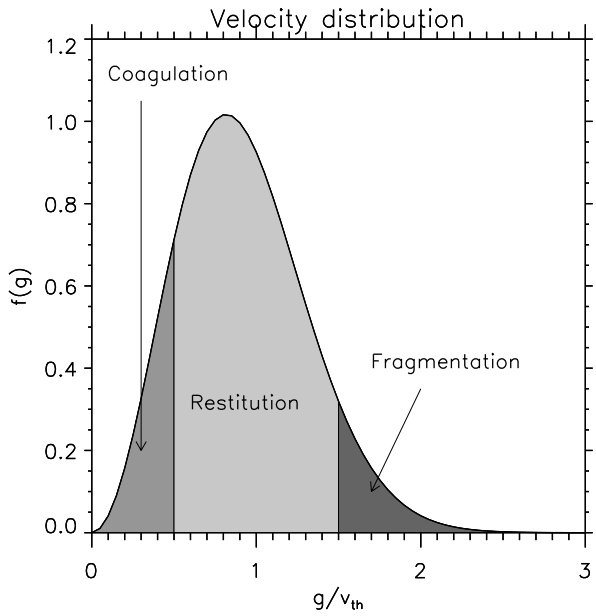

Figure 6.1: Maxwellian velocity distribution $f(g)$ of the collisions velocities of the aggregates. Note, impact speeds of the range of $\mathrm{mm\,s^{-1}}$ up to $\mathrm{cm\,s^{-1}}$ are expected in Saturn's rings (mean velocity $\approx 5\,\mathrm{mm\,s^{-1}}$).

The Maxwellian velocity dispersion, $f(g)$ (Fig. 6.1), is a possible reasonable estimate for the impact velocity distribution of the ring particles (neglecting systematic motions). The lower end and the upper tail of this distribution mark the velocity ranges where aggregation and fragmentation may occur. The gap between aggregation and fragmentation velocities marks the range of collisional restitutions for the majority of the collisions.

Molecular dynamics simulations – including integration of the collision dynamics of the constituents of two colliding aggregates – would be necessary in order to determine the domains of fragmentation, restitution and aggregation more precisely. However, our results already provide enough information in order to undertake kinetic calculations for the evolution of the size distribution, i.e. the domains of the collision integrals

for coagulation, restitution and fragmentation can now be estimated.

The influence of $v_{\rm th}$ on the balance of fragmentation and coagulation has already been discussed. However the size distribution of the ring particles as well as the fragmentation and coagulation processes itself influence the establishment of the particle velocity distribution. We have not investigated this effect in this work, but it would be worthwhile to do it in future.

The specific binding energy, $Q^\star$, derived in this paper, is related to the mean specific kinetic energy of the ring particles. With the help of $Q^\star$ we can derive expressions for the aggregation and fragmentation speeds $g_{\rm agg} < g < g_{\rm frag}$, which has been done for $g_{\rm frag}$ in Chapter 5. For two colliding aggregates of the same size the fragmentation velocity is inversely proportional to the aggregate size, $g_{\rm frag} \propto R^{-1}$, the same relation should also hold for $g_{\rm agg}$. When a steady size distribution is established the fragmentation and aggregation rates will minimize. This will occur when the mean kinetic energy $\propto v_{\rm th}^2$ approaches the specific binding energy $Q^\star$. Therefore, we arrive at the hypothesis, that the mean thermal velocity evolves dynamically, with $v_{\rm th} \propto R^{-1/2}$. Other velocity distributions, which could be gained from equipartition, where $v_{\rm th} \propto R^{-3/2}$, or the assumption of a size independent velocity distribution, would result in slopes which are steep or shallow gradient, which would lead again to enhanced aggregation/fragmentation rates.

Our hypothesis proposes an adaptation of the velocity distribution to the radial dependence of $Q^\star$. Similar phenomena are known in physics, for example the self-organized criticality (SOC, Bak et al., 1987). An example of a SOC is the steady dumping of sand on top of a sand pile, which then triggers a series of avalanches. This guarantees that the angle of repose at the pile-edges remains within a narrow range around a self-organized critical value. The slightest disturbances can generate new, even arbitrary

small avalanches that maintain the critical angle.

Finally we want to consider a large aggregate in a soup of constituents with a mean impact velocity, g, where in a certain case we have $g \approx v_{\mathrm{th}}$. The aggregate will grow if the kinetic energy of the constituent is smaller than the specific contact energy, $Q - Q^{\star}(R)$, for a body of radius R, otherwise higher kinetic energies could lead to a split off bound constituents. Thus, the aggregate can grow or shrink if $g < g_{\mathrm{c}}$ or $g > g_{\mathrm{c}}$, respectively. The critical velocity, g_{c}, is defined by $g_{\mathrm{c}}^2/2 = Q - Q^{\star}$ and is an unstable point where the aggregate would neither grow nor shrink. This is analog to droplet formation in a supersaturated gas (clouds) known from equilibrium thermodynamics which leads to a similar relation with $\mu_{drop} + (2m/\rho)(\sigma/R) - \mu_{gas} = 0$. Here μ denotes the chemical potential of droplet and gas together with its surface tension σ/R. Here $\mu_{drop} - \mu_{gas}$ corresponds to $g_{\mathrm{c}}^2/2 - Q$ and the surface tension to $Q^{\star}$.

Royer et al. (2009) have shown that for adhering granular particles such a surface tension does also exist. Our numerically designed aggregates already contain this energetic part, which is easily demonstrated by the investment of energy in order to split an aggregate (to create new surfaces) owing to the contact adhesion. Of course, this analogy is quite formal, because in the case of the ring aggregate ensemble dissipation leads to a quick cooling ($T \to 0$) of the aggregate so that an equal temperature for all phases is not given here.

6.1 Conclusions

We have analytically and numerically studied the specific binding energies of aggregates held together by gravity and surface contact forces like adhesion and found a qualitative agreement to previous works (e.g. Love and Ahrens (1996); Davis et al.

(1985). We have also shown that aggregate resistivity actively contributes to determine the size distribution in planetary rings. In the case of Saturn's rings we estimate the upper size cut-off to be on the order of tens of meters which is in quantitatively good agreement with observations. Further, aggregate sizes, resistivity, and both aggregation and fragmentation threshold velocities provide direct input for parameters which are crucial in undertaking kinetic studies of the size and velocity distributions of granular systems such as planetary rings.

Appendix A

Adhesive-elastic contact energy

The energy required to separate two particles s_1 and s_2 - the energy of one "adhesive bond" - comprises both the mechanical (elastic) energy of particle deformation u_{elas} and the non-mechanical (adhesive) energy u_{add}. Following Brilliantov et al. (2007) it may be shown that for the equilibrium contact u_{elas} reads

$$u_{\mathrm{elas}} = \frac{a^5}{15 D s_{\mathrm{eff}}^2} = \frac{6^{5/3}}{15} \left(\pi^5 D^2 \gamma^5 s_{\mathrm{eff}}^4 \right)^{1/3}, \tag{A.1}$$

where $s_{\mathrm{eff}} = s_1 s_2 / (s_1 + s_2)$ denotes the effective particle size, γ twice the surface free energy γ_0. The bulk material constants Young's modulus Y and Poisson ratio ν have been combined into a single constant $D = 3(1-\nu^2)/(2Y)$, implicitly assuming that all particles are made of the same material. To put the non-mechanical adhesive energy into mechanical context, we need to consider the interactions between the two particles on the microscopic, interatomic level. We assume that they interact by the Lennard-

Jones potential (the particular form of the inter-atomic potential is not important)

$$u_{\rm ij} = 4\varepsilon \left[\left(\frac{\sigma_\diamond}{r_{\rm ij}} \right)^{12} - \left(\frac{\sigma_\diamond}{r_{\rm ij}} \right)^{6} \right], \tag{A.2}$$

where ε characterizes the interaction strength, $\sigma_\diamond$ is the characteristic size of particles atoms and $r_{\rm ij}$ is the interatomic distance between the i-th atom of the test particle and j-th atom of the particle of the aggregate. Then the interaction energy between the two particles is equal to the sum over all atoms i and j, which may be approximated by the continuum integral over particles' material. After rigorous analysis we find

$$u_{\rm adh} = -\int_d^{2s_1} dz_1 \int_d^{2s_2} dz_2 \int_0^{a(z_1)} r_1 dr_1 \int_0^{a(z_2)} r_2 dr_2 \int_0^{2\pi} d\phi \frac{8\pi\varepsilon\sigma_\diamond^6 \rho_\diamondsuit^2}{\left((z_1+z_2)^2 + r_1^2 + r_2^2 - 2r_1 r_2 \cos\phi\right)^3}. \tag{A.3}$$

Here $\rho_\diamondsuit$ is the number density of atoms of the particle material, z_1 and z_2 are the distances (in normal direction) from the plane of contact, where $z_1 = z_2 = 0$, $d = 2^{1/6}\sigma_\diamond$ is the equilibrium distance between atoms, and $a_{1/2}(z)$ is the shape of the deformed spheres (that is, of our particles) around the contact zone. We further assume that the inter-particle contact corresponds to the equilibrium contact with $a(z=0) = a_{\rm eq}$ given by (Brilliantov et al., 2007)

$$a_{\rm eq}^3 = 6\pi\gamma D s_{\rm eff}^2 \tag{A.4}$$

The integration in Eq. (A.3) is performed over the total particle volume (s_1 and s_2 are the particle radii of a pair in contact which define $s_{\rm eff}$).

To obtain an analytical estimate of the integral in Eq. (A.3) we approximate the shape of the deformed particle $a(z)$ with the relation,

$$a_{\rm k}(z_{\rm k})^2 = a^2 + s_{\rm k}^2 - (s_{\rm k} - z_{\rm k})^2 \qquad \text{for} \qquad k = 1,2. \tag{A.5}$$

This approximation satisfies $a_{\rm k}(z_{\rm k}=0)=a_{\rm eq}$ and $a_{\rm k}^2(z_{\rm k}=s_{\rm k})=a_{\rm eq}^2+s_{\rm k}^2\approx s_{\rm k}^2$, since $s_{\rm k}\gg a_{\rm eq}$, that is at the heights $z_{\rm k}=s_{\rm k}$ the deformation vanishes.

If we further assume that the equilibrium contact area $\pi a_{\rm eq}^2$ is much larger than the atomic area, $\pi\sigma_\diamond^2$, we may integrate over r_1 and over r_2 with the acceptable accuracy from zero to infinity. While keeping only linear terms in the expansion in small parameter $d/s_{1/2}$ and assuming for simplicity that $s_1=s_2=s$ we find after rigorous calculations

$$u_{\rm adh}=-\frac{A_{\rm H}a_{\rm eq}^2}{12D_0^2}\left[1+\frac{D_0}{2s}+\frac{3D_0 s}{a_{\rm eq}^2}\right], \tag{A.6}$$

where $D_0=2d=2\cdot 2^{1/6}\sigma_\diamond$ is the equilibrium distance between the centers of atoms of the two surfaces and

$$A_H=4\varepsilon\sigma_\diamond^6\pi^2\rho^2 \tag{A.7}$$

is the Hamaker constant (Israelachvili, 2011). Taking into account that the Hamaker constant is related to the surface tension γ_0 as (Israelachvili, 2011)

$$\gamma_{\rm surf}=\frac{A_H}{24\pi D_0^2}, \tag{A.8}$$

and that the adhesive energy γ, introduced above, is twice the surface tension, $\gamma=2\gamma_0$ (Brilliantov et al., 2007), we finally obtain

$$u_{\rm adh}=-\pi a_{\rm eq}^2\gamma\left[1+\frac{D_0}{2s}+\frac{3D_0 s}{a_{\rm eq}^2}\right]., \tag{A.9}$$

In the limit of $D_0/s\to 0$ this is consistent with the simple estimate $\pi\gamma a_{\rm eq}^2$ as follows from thermodynamics. Thus,

$$E_{\rm A}^{(2)}=u_{\rm adh}+u_{\rm elas}=-\pi\gamma a_{\rm eq}^2+\frac{a_{\rm eq}^5}{15Ds_{\rm eff}^2}. \tag{A.10}$$

Using Eq. (A.4) for a_{eq}, we may write

$$E_{\mathrm{A}}^{(2)} = -\frac{6^{2/3}}{5}\left(\pi^5 D^2 \gamma^5 s_{\mathrm{eff}}^4\right)^{1/3} = A^{(\mathrm{ij})}\, s_{\mathrm{eff}}^{4/3}\,, \tag{A.11}$$

where $A^{(\mathrm{ij})} \approx 4.45\,(D^2\gamma^5)^{1/3}$ with $[A^{(\mathrm{ij})}] = \mathrm{N\,m^{-1/3}}$.

References

Albers, N., 2006. On the relevance of particle adhesion: Applications to saturns rings. Ph.D. thesis, Institut für Physik der Universität Potsdam.

Albers, N., Spahn, F., mar 2006. The influence of particle adhesion on the stability of agglomerates in Saturn's rings. Icarus 181, 292–301.

Bak, P., Tang, C., Wiesenfeld, K., Jul 1987. Self-organized criticality: An explanation of the 1f noise. Phys. Rev. Lett. 59, 381–384.

Barbara, J. M., Esposito, L. W., Nov. 2002. Moonlet collisions and the effects of tidally modified accretion in saturn's f ring. Icarus 160, 161–171.

Benz, W., Asphaug, E., Nov. 1999. Catastrophic disruptions revisited. Icarus 142, 5–20.

Beurle, K., Murray, C., Williams, G., Evans, M., Cooper, N., Agnor, C., 2010. Direct evidence for gravitational instability and moonlet formation in saturn's rings. The Astrophysical Journal Letters 718, L176.

Bodrova, A., Schmidt, J., Spahn, F., Brilliantov, N., Mar. 2012. Adhesion and collisional release of particles in dense planetary rings. Icarus 218, 60–68.

Bridges, F. G., Hatzes, A., Lin, D. N. C., May 1984. Structure, stability and evolution of saturn's rings. Nature 309, 333–335.

Brilliantov, N. V., Albers, N., Spahn, F., Pöschel, T., Nov. 2007. Collision dynamics of granular particles with adhesion. Physical Review E 76 (5), 051302–+.

Brilliantov, N. V., Spahn, F., Hertzsch, J.-M., Pöschel, T., mai 1996. Model for collisions in granular gases. Physical Review E 53, 5382–5392.

Chokshi, A., Tielens, A. G. G. M., Hollenbach, D., Apr. 1993. Dust coagulation. Astrophysical Journal 407, 806–819.

Colwell, J. E., Cooney, J. H., Esposito, L. W., Sremčević, M., Apr. 2009. Density waves

in cassini uvis stellar occultations. 1. the cassini division. Icarus 200, 574–580.

Colwell, J. E., Esposito, L. W., Sremčević, M., Apr. 2006. Self-gravity wakes in saturn's a ring measured by stellar occultations from cassini. Geophysical Research Letters 33, 7201–+.

Colwell, J. E., Esposito, L. W., Sremčević, M., Stewart, G. R., McClintock, W. E., Sep. 2007. Self-gravity wakes and radial structure of saturn's b ring. Icarus 190, 127–144.

Cuzzi, J., Burns, J., Charnoz, S., Clark, R., Colwell, J., Dones, L., Esposito, L., Filacchione, G., French, R., Hedman, M., et al., 2010. An evolving view of satun's dynamic rings. Science 327 (5972), 1470.

Cuzzi, J., Clark, R., Filacchione, G., French, R., Johnson, R., Marouf, E., Spilker, L., 2009. Ring particle composition and size distribution. Saturn from Cassini-Huygens 1, 459.

Daisaka, H., Ida, S., Nov. 1999. Spatial structure and coherent motion in dense planetary rings induced by self-gravitational instability. Icarus 51, 1195–1213.

Davis, D. R., Chapman, C. R., Weidenschilling, S. J., Greenberg, R., Jul. 1985. Collisional history of asteroids: Evidence from vesta and the hirayama families. Icarus 63, 30–53.

Davis, D. R., Weidenschilling, S. J., Chapman, C. R., Greenberg, R., May 1984. Saturn ring particles as dynamic ephemeral bodies. Science 224, 744–747.

Dohnanyi, J. S., May 1969. Collisional Model of Asteroids and Their Debris. JGR 74, 2531–+.

Dominik, C., Tielens, A. G. G. M., May 1997. The physics of dust coagulation and the structure of dust aggregates in space. The Astrophysical Journal 480, 647–+.

Dougherty, M. K., Esposito, L. W., Krimigis, S. M., 2009. Saturn from Cassini-Huygens.

Esposito, L., Albers, N., Meinke, B. K., Sremčević, M., M., Madhusudhanan, P., Colwell, J. E., Jerousek, R. G., 2011. A predetor-prey model for moon-triggered clumping in saturn's rings. Icarus.

Esposito, L. W., Dec. 2002. Planetary rings.

Reports on Progress in Physics 65, 1741–1783.

Esposito, L. W., Meinke, B. K., Colwell, J. E., Nicholson, P. D., Hedman, M. M., Mar. 2008. Moonlets and clumps in saturn's f ring. Icarus 194, 278–289.

French, R. G., Nicholson, P. D., Jun. 2000. Saturn's rings ii. particle sizes inferred from stellar occultation data. Icarus 145, 502–523.

French, R. G., Salo, H., McGhee, C. A., Dones, L., Aug. 2007. Hst observations of azimuthal asymmetry in saturn's rings. Icarus 189, 493–522.

Goldreich, P., Tremaine, S. D., May 1978. The velocity dispersion in Saturn's rings. Icarus 34, 227–239.

Gundlach, B., Kilias, S., Beitz, E., Blum, J., 2011. Micrometer-sized ice particles for planetary-science experiments-i. preparation, critical rolling friction force, and specific surface energy. Icarus.

Güttler, C., Blum, J., Zsom, A., Ormel, C., Dullemond, C., 2010. The outcome of protoplanetary dust growth: pebbles, boulders, or planetesimals? Astronomy & Astrophysics 513.

Hatzes, A. P., Bridges, F., Lin, D. N. C., Sachtjen, S., Jan. 1991. Coagulation of particles in Saturn's rings - Measurements of the cohesive force of water frost. Icarus 89, 113–121.

Hedman, M. M., Nicholson, P. D., Salo, H., Wallis, B. D., Buratti, B. J., Baines, K. H., Brown, R. H., Clark, R. N., Jun. 2007. Self-gravity wake structures in saturn's a ring revealed by cassini vims. Astrophysical Journal 133, 2624–2629.

Holsapple, K. A., 2009. On the "strength" of the small bodies of the solar system: A review of strength theories and their implementation for analyses of impact disruptions. Planetary and Space Science, 127–141.

Housen, K. R., Holsapple, K. A., Mar. 1990. On the fragmentation of asteroids and planetary satellites. Icarus 84, 226–253.

Israelachvili, J., 2011. Intermolecular and Surface Forces. Academic Press.

Johnson, K. L., Kendall, K., Roberts, A. D., sep 1971. Surface energy and the contact

of elastic solids. Proceedings of the Royal Society of London. Series A, Mathematical and Physical Sciences 324 (1558), 301–313.

Kempf, S., Pfalzner, S., Henning, T. K., Oct. 1999. N-partcile-simulations of dust growth. i. growth driven by brownian motion. Icarus 141, 388–398.

Kolokolova, L., Kimura, H., Kiselev, N., Rosenbush, V., Mar. 2007. Two different evolutionary types of comets proved by polarimetric and infrared properties of their dust. Astronomy & Astrophysics 463, 1189–1196.

Krivov, A. V., Mann, I., Krivova, N. A., Oct. 2000. Size distributions of dust in circumstellar debris discs. Astronomy & Astrophysics 362, 1127–1137.

Krivov, A. V., Sremčević, M., Spahn, F., Mar. 2005. Evolution of a Keplerian disk of colliding and fragmenting particles: a kinetic model with application to the Edgeworth Kuiper belt. Icarus 174, 105–134.

Lobanov, M., Bogatyreva, N., Galzitskaya, O., 2008. Radius of gyration as an indicator of protein structure compactness. Molecular Biology 42 (4), 623–628.

Longaretti, P., 1989. Saturn's main ring particle size distribution: An analytic approach. Icarus 81 (1), 51–73.

Love, S. G., Ahrens, T. J., Nov. 1996. Catastrophic impacts on gravity dominated asteroids. Icarus 124, 141–155.

Marouf, E., Leonard Tyler, G., Zebker, H., Simpson, R., Eshleman, V., 1983. Particle size distributions in Saturn's rings from Voyager 1 radio occultation. Icarus 54 (2), 189–211.

Meinke, B. K., Esposito, L. W., Albers, N., Sremčević, M., Mar. 2012. Classification of f ring features observed in cassini uvis occultations. Icarus 218, 545–554.

Moreno-Atanasio, R., Ghadiri, M., Jan. 2006. Mechanistic analysis and computer simulation of impact breakage of agglomerates: Effect of surface energy. Chemical Engineering Science 124, 2476–2481.

Mrafko, P., Duhaj, P., Jun. 1974. Analysis of an aggregate of hard spheres. Physica Status Solidi Applied Research 23, 583–589.

Mukai, T., Ishimoto, H., Kozasa, T., Blum, J., Greenberg, J. M., 1992. Radiation pressure forces of fluffy porous grains. Astronomy & Astrophysics, 315–320.

Murray, C., Dermott, S., 1999. Solar system dynamics. Cambridge Univ Pr.

Murray, C. D., Beurle, K., Cooper, N. J., Evans, M. W., Williams, G. A., Charnoz, S., Jun. 2008. The determination of the structure of saturn's f ring by nearby moonlets. Nature 453, 739–744.

Murray, C. D., Chavez, C., Beurle, K., Cooper, N., Evans, M. W., Burns, J. A., Porco, C. C., Oct. 2005. How Prometheus creates structure in Saturn's F ring. Nature 437, 1326–1329.

Nicholson, P. D., Hedman, M. M., Clark, R. N., Showalter, M. R., Cruikshank, D. P., Cuzzi, J. N., Filacchione, G., Capaccioni, F., Cerroni, P., Hansen, G. B., Sicardy, B., Drossart, P., Brown, R. H., Buratti, B. J., Baines, K. H., Coradini, A., Jan. 2008. A close look at saturn's rings with cassini vims. Icarus 193, 182–212.

Perrine, R. P., Richardson, D. C., Scheeres, D. J., Apr. 2011. A numerical model of cohesion in planetary rings. Icarus 212, 719–735.

Porco, C., Thomas, P., Weiss, J., Richardson, D., 2007. Saturn's Small Inner Satellites: Clues to Their Origins. Science 318 (5856), 1602.

Richardson, D. C., Jun. 1995. A self-consistent numerical treatment of fractal aggregate dynamics. Icarus 115, 320–+.

Robbins, S. J., Stewart, G. R., Lewis, M. C., Colwell, J. E., Sremcevic, M., 2009. Estimating the masses of saturn's a and b rings from high-optical depth n-body simulations and stellar occultations. Icarus In Press, Corrected Proof.

Royer, J., Evans, D., Oyarte, L., Guo, Q., Kapit, E., Möbius, M., Waitukaitis, S., Jaeger, H., 2009. High-speed tracking of rupture and clustering in freely falling granular streams. Nature 459 (7250), 1110–1113.

Salo, H., Oct. 1992. Gravitational wakes in saturn's rings. Nature 359, 619–621.

Salo, H., Oct. 1995. Simulations of dense planetary rings. iii. self-gravitating identical particles. Icarus 117, 287–312.

REFERENCES

Scheeres, D. J., Hartzell, C. M., Sánchez, P., Swift, M., Dec. 2010. Scaling forces to asteroid surfaces: The role of cohesion. Icarus 210, 968–984.

Schlingloff, H., 2005. Astronautical engineering: An introduction to the technology of spaceflight. Ingenieurbüro Dr. Schlingloff Publications.

Seipenbusch, M., Toneva, P., Peukert, W., Weber, A. P., 2007. Impact fragmentation of metal nanoparticle agglomerates. Particle & Particle Systems Characterization, 193–200.

Shen, Y., Draine, B., Johnson, E., 2008. Modeling porous dust grains with ballistic aggregates. i. geometry and optical properties. The Astrophysical Journal 689, 260.

Shen, Y., Draine, B., Johnson, E., 2009. Modeling porous dust grains with ballistic aggregates. ii. light scattering properties. The Astrophysical Journal 696, 2126.

Showalter, M. R., Pollack, J. B., Ockert, M. E., Doyle, L. R., Dalton, J. B., Dec. 1992. A photometric study of saturn's f ring. Icarus 100, 394–411.

Spahn, F., Albers, N., Sremcevic, M., Thornton, C., aug 2004. Kinetic description of coagulation and fragmentation in dilute granular particle ensembles. Europhysics Letters 67, 545–551.

Spahn, F., Schmidt, J., mar 2006. Planetary science: Saturn's bared mini-moons. Nature 440, 614–615.

Spahn, F., Sponholz, H., Jun. 1989. Existence of moonlets in saturn's rings inferred from the optical depth profile. Nature 339, 607–+.

Sremčević, M., dec 2007. Propellers: Theory and observation. AGU Fall Meeting Abstracts.

Sremčeivć, M., Schmidt, J., Salo, H., Seiß, M., Spahn, F., Albers, N., 2007. A belt of moonlets in saturn's a ring. Nature 449 (7165), 1019–1021.

Tiscareno, M., Burns, J., Nicholson, P., Hedman, M., Porco, C., 2007. Cassini imaging of saturn's rings:: Ii. a wavelet technique for analysis of density waves and other radial structure in the rings. Icarus 189 (1), 14–34.

Tiscareno, M. S., Burns, J. A., Hedman, M. M., Porco, C. C., Weiss, J. W., Dones, L., Richardson, D. C., Murray, C. D., Mar. 2006. 100-metre-diameter moonlets in saturn's a ring from observations of propeller structures. Nature 440, 648–650.

Vold, M., 1959. A numerical approach to the problem of sediment volume 1. Journal of colloid science 14 (2), 168–174.

Wada, K., Tanaka, H., Suyama, T., Kimura, H., Yamamoto, T., Apr. 2008. Numerical Simulation of Dust Aggregate Collisions. II. Compression and Disruption of Three-Dimensional Aggregates in Head-on Collisions. Astrophysical Journal 677, 1296–1308.

Weidenschilling, S. J., Chapman, C. R., Davis, D. R., Greenberg, R., 1984. Ring particles - collisional interactions and physical nature. In: Greenberg, R., Brahic, A. (Eds.), IAU Colloq. 75: Planetary Rings. pp. 367–415.

Winter, O. C., Mourao, D. C., Giuliatti Winter, S. M., Spahn, F., da Cruz, C., 2007. Moonlets wandering on a leash-ring. Monthly Notices of the Royal Astronomical Society: Letters 380 (1), L54–L57.

Zebker, H. A., Marouf, E. A., Tyler, G. L., Dec. 1985. Saturn's rings - particle size distributions for thin layer model. Icarus 64, 531–548.